

**1 Solar wind driving of magnetospheric ULF waves: Field line**  
**2 resonances driven by dynamic pressure fluctuations**

S. G. Claudepierre,<sup>1,2</sup> M. K. Hudson,<sup>1</sup> W. Lotko,<sup>3</sup> J. G. Lyon,<sup>1</sup> and R. E. Denton<sup>1</sup>

---

S. G. Claudepierre, The Aerospace Corporation, P.O. Box 92957, MS: M2-260, Los Angeles, CA 90009-2957, USA. (seth.claudepierre@gmail.com)

R. E. Denton, Department of Physics and Astronomy, Dartmouth College, Hanover, NH 03755, USA. (richard.e.denton@dartmouth.edu)

M. K. Hudson, Department of Physics and Astronomy, Dartmouth College, Hanover, NH 03755, USA. (mary.k.hudson@dartmouth.edu)

W. Lotko, Thayer School of Engineering, Dartmouth College, Hanover, NH 03755, USA. (william.lotko@dartmouth.edu)

J. G. Lyon, Department of Physics and Astronomy, Dartmouth College, Hanover, NH 03755, USA. (john.g.lyon@dartmouth.edu)

<sup>1</sup>Department of Physics and Astronomy,

arXiv:1010.3994v1 [physics.space-ph] 19 Oct 2010

3 **Abstract.** Several observational studies suggest that solar wind dynamic pres-  
4 sure fluctuations can drive magnetospheric ultra-low frequency (ULF) waves on  
5 the dayside. To investigate this causal relationship, we present results from Lyon-  
6 Fedder-Mobarry (LFM) global, three-dimensional magnetohydrodynamic (MHD)  
7 simulations of the solar wind-magnetosphere interaction. These simulations are  
8 driven with synthetic solar wind input conditions, where idealized ULF dynamic  
9 pressure fluctuations are embedded in the upstream solar wind. In three of the  
10 simulations, a monochromatic, sinusoidal ULF oscillation is introduced into the  
11 solar wind dynamic pressure time series. In the fourth simulation, a continuum  
12 of ULF fluctuations over the 0-50 mHz frequency band is introduced into the  
13 solar wind dynamic pressure time series. In this numerical experiment, the ide-  
14 alized solar wind input conditions allow us to study only the effect of a fluc-  
15 tuating solar wind dynamic pressure, while holding all of the other solar wind  
16 driving parameters constant. We show that the monochromatic solar wind dy-  
17 namic pressure fluctuations drive toroidal mode field line resonances (FLRs) on

---

Dartmouth College, Hanover, New Hampshire,  
USA.

<sup>2</sup>Now at The Aerospace Corporation, Los  
Angeles, CA, USA.

<sup>3</sup>Thayer School of Engineering, Dartmouth  
College, Hanover, New Hampshire, USA.

18 the dayside, at locations where the upstream driving frequency matches a lo-  
19 cal field line eigenfrequency. In addition, we show that the continuum of up-  
20 stream solar wind dynamic pressure fluctuations drives a continuous spectrum  
21 of toroidal mode FLRs on the dayside. The characteristics of the simulated FLRs  
22 agree well with FLR observations, including a phase reversal radially across a  
23 peak in wave power, a change in the sense of polarization across the noon merid-  
24 ian, and a net flux of energy into the ionosphere.

## 1. Introduction

25 Observations of magnetospheric ultra-low frequency (ULF) pulsations are typically inter-  
26 preted as the observable signature of magnetohydrodynamic (MHD) waves propagating in the  
27 magnetosphere [*Southwood and Hughes, 1983*]. In this work, ‘ULF’ refers to frequencies in  
28 the 0.5-50 mHz range, though we make no distinction between continuous (Pc) and irregular  
29 (Pi) pulsations [e.g. *Jacobs et al., 1964*]. Magnetospheric ULF pulsations can be generated by  
30 a variety of mechanisms, which are often classified as either internal or external mechanisms.  
31 Unstable plasma configurations in the magnetosphere can lead to a local (i.e. internal) gener-  
32 ation of ULF pulsations [e.g. *Hasegawa, 1969; Hughes et al., 1978*]. In this work, however,  
33 we are concerned with magnetospheric ULF pulsations driven by the solar wind (i.e. exter-  
34 nally). Two examples of external drivers of magnetospheric ULF pulsations are [*Takahashi and*  
35 *Ukhorskiy, 2007*]: velocity shear at the magnetopause (e.g. the Kelvin-Helmholtz instability)  
36 and ULF fluctuations in the solar wind dynamic pressure. Observations of tailward propagating  
37 surface waves near the dawn and dusk flank magnetopause are often attributed to the Kelvin-  
38 Helmholtz instability [*Fairfield, 1979; Sckopke et al., 1981; Hones et al., 1981; Couzens et al.,*  
39 *1985*]. Many of the observational features of these magnetopause surface waves agree well  
40 with theoretical and numerical studies of the Kelvin-Helmholtz instability [*Walker, 1981; Pu*  
41 *and Kivelson, 1983; Claudepierre et al., 2008*]. However, in this work, we focus on the second  
42 external driving mechanism, ULF fluctuations in the solar wind dynamic pressure.

43 Several observational studies have shown that ULF fluctuations in the solar wind dynamic  
44 pressure can drive corresponding ULF fluctuations in the magnetosphere. For example, *Kepko*  
45 *et al.* [2002] and *Kepko and Spence* [2003] studied several events where discrete frequency,

46 ULF fluctuations were observed in the solar wind number density. A one-to-one correspon-  
47 dence was observed between the solar wind number density oscillation frequencies and oscilla-  
48 tion frequencies in dayside magnetic field measurements from the GOES satellite. The authors  
49 concluded that the fluctuations in the solar wind number density (or dynamic pressure) drove  
50 the corresponding fluctuations in the magnetosphere. *Korotova and Sibeck [1995]* and *Mat-*  
51 *suoka et al. [1995]* used simultaneous ground based, geosynchronous, and upstream solar wind  
52 measurements to show that periodic fluctuations in the solar wind dynamic pressure drove ULF  
53 pulsations in the magnetosphere. *Sarafopoulos [1995]* reported on a magnetotail lobe oscillation  
54 driven by a corresponding fluctuation in the solar wind dynamic pressure. Recent work [*Viall*  
55 *et al., 2009*] has argued that approximately half of the variations observed in magnetospheric  
56 ULF waves are driven by solar wind dynamic pressure fluctuations. While these observational  
57 studies have shown that periodic fluctuations in the solar wind dynamic pressure can drive mag-  
58 netospheric ULF pulsations in general, other studies have considered the possibility that solar  
59 wind dynamic pressure fluctuations can drive field line resonances in the magnetospheric cavity  
60 [*Takahashi et al., 1988; Potemra et al., 1989; Southwood and Kivelson, 1990; Stephenson and*  
61 *Walker, 2002*].

62 A field line resonance (FLR) is the resonant Alfvénic oscillation of a closed geomagnetic field  
63 line, whose foot points lie in the ionosphere. *Dungey [1955]* was perhaps the first to suggest that  
64 ground based magnetometer observations of discrete frequency fluctuations were the signature  
65 of MHD standing waves on closed geomagnetic field lines. The discrete frequency oscillations  
66 arise from the restriction to an integral number of half-wavelengths along the field line. This  
67 scenario is illustrated schematically in Figure 1 (after *Southwood and Hughes [1983]*). The left  
68 column shows the standing wave mode structure for the fundamental, second and third harmon-

69 ics for the electric field oscillation and the right column shows the corresponding mode structure  
70 for the magnetic field oscillation. To simplify the comparisons with our MHD simulations, os-  
71 cillation amplitude is plotted as a non-negative quantity and, thus, there is no phase information  
72 depicted in Figure 1. The location of the geomagnetic equatorial plane is indicated by a vertical  
73 dashed line in each column and is labeled ‘eq.’ A perfectly conducting ionosphere is assumed at  
74 the field line foot points, which are labeled ‘iono’ in the figure. At the perfectly conducting (i.e.  
75 perfectly reflecting) ionospheric boundaries, the electric field oscillation amplitude goes to zero  
76 and the derivative of the magnetic field oscillation amplitude goes to zero [Zhu and Kivelson,  
77 1989]. This imposes half-wavelength standing waves along the field line. We note that while  
78 the real ionosphere is not a perfect conductor, magnetospheric FLR mode structure is typically  
79 well-approximated in this limit [Southwood and Hughes, 1983].

80 Ground-based magnetometer observations of ULF pulsations often show a peak in wave  
81 power at a particular latitude [Samson et al., 1971; Samson and Rostoker, 1972; Walker et al.,  
82 1979; Ruohoniemi et al., 1991]. The FLR theories of Chen and Hasegawa [1974] and South-  
83 wood [1974] predict that this feature is due to the coupling of compressional wave energy into  
84 the shear Alfvén mode at a spatial location where the local field line eigenfrequency matches the  
85 frequency of the compressional source. The MHD wave equations that describe the coupling  
86 between the fast compressional mode and the shear Alfvén mode are complicated and have  
87 not been completely solved analytically, even in a simple dipole geometry. We note, however,  
88 that some analytic work has been done in nonuniform geometries (including a dipole), lead-  
89 ing to approximate solutions [c.f. Goedbloed, 1975; Inhester, 1986; Chen and Cowley, 1989;  
90 Mond et al., 1990; Wright and Thompson, 1994]. The equations decouple, however, in the limit  
91 of large and small azimuthal mode number,  $m$ , and describe three modes of oscillation: the

92 poloidal Alfvén mode, the toroidal Alfvén mode, and the fast mode [*Radoski and Carovillano,*  
93 1966; *Singer et al.*, 1981]. In the poloidal mode of oscillation ( $m \rightarrow \infty$ ), dipole magnetic  
94 field lines oscillate radially in a fixed meridional plane. Thus, in cylindrical polar coordinates,  
95 the oscillations are in the  $v_r$ ,  $B_r$ , and  $E_\varphi$  field components. In the toroidal mode of oscillation  
96 ( $m \rightarrow 0$ ), each  $L$ -shell oscillates azimuthally and the oscillations are in the  $v_\varphi$ ,  $B_\varphi$  and  $E_r$  field  
97 components. In the fast mode of oscillation ( $m \rightarrow 0$ ), the oscillations are in the  $v_r$ ,  $B_r$ ,  $B_\parallel$  and  
98  $E_\varphi$  field components.

99 The Kelvin-Helmholtz instability at the magnetopause is often cited as the source of compres-  
100 sional energy required for the excitation of FLRs [e.g. *Chen and Hasegawa*, 1974; *Southwood,*  
101 1974]. However, as noted above, several observational studies have suggested that FLRs can  
102 be driven by fluctuations in the solar wind dynamic pressure. For example, *Stephenson and*  
103 *Walker* [2002] reported on HF radar observations of discrete frequency FLRs, where the same  
104 frequencies were observed in solar wind dynamic pressure fluctuations. *Takahashi et al.* [1988]  
105 reported on an observation of a toroidal mode FLR and the authors suggested that the FLR was  
106 driven by a series of solar wind pressure disturbances. *Potemra et al.* [1989] considered simulta-  
107 neous observations of the solar wind, measured by the IMP 8 satellite, and the magnetosphere,  
108 measured by ground based magnetometers and the AMPTE satellite. The authors concluded  
109 that a monochromatic fluctuation in the solar wind number density launched a tailward travel-  
110 ing wave train in the magnetosphere that excited local FLRs. In addition to these observational  
111 studies, the theoretical work of *Southwood and Kivelson* [1990] studied the magnetospheric  
112 response to solar wind dynamic pressure changes. They found both FLRs and a global, com-  
113 pressional eigenoscillation of the entire magnetospheric cavity, known as the ‘cavity mode,’

114 in the response. These studies all suggest that solar wind dynamic pressure fluctuations can  
115 provide the compressional source of energy required for the excitation of FLRs.

116 In this work, we use global MHD simulations to study the role that solar wind dynamic  
117 pressure fluctuations play in the generation of magnetospheric ULF pulsations. We show that  
118 monochromatic ULF fluctuations in the solar wind dynamic pressure can drive toroidal mode  
119 field line resonances in the simulation magnetosphere. In addition, we show that fluctuations  
120 over a continuum of ULF frequencies in the solar wind dynamic pressure can drive a continu-  
121 ous spectrum of toroidal mode FLRs. The remainder of this paper is structured as follows: in  
122 Section 2, we discuss the Lyon-Fedder-Mobarry global MHD simulation, which is the primary  
123 tool used in this work and, in Section 3, we present the simulation results. Section 4 provides  
124 a detailed discussion of the simulated FLRs, including a comparison with some general char-  
125 acteristics of FLR observations. Finally, in Section 5, we provide a summary of the results and  
126 offer some concluding remarks.

## 2. Methodology

127 The Lyon-Fedder-Mobarry (LFM) code solves the single fluid, ideal magnetohydrodynamic  
128 (MHD) equations on a three-dimensional grid to simulate the interaction between the solar  
129 wind, magnetosphere, and ionosphere. We discuss the features of the LFM simulation that are  
130 the most pertinent to this study; a more detailed code description, including a discussion of the  
131 accuracy of the solution, can be found in *Lyon et al.* [2004].

132 The LFM computational grid is a non-Cartesian, distorted spherical mesh, which, in this  
133 study, contains 106x48x64 grid cells. This translates to a spatial resolution of roughly 0.25  
134  $R_E$  in the inner magnetosphere ( $r < 6.6 R_E$ ), though the spacing is not uniform. The outer  
135 boundary condition in the LFM simulation is the solar wind, which is input into the simulation



136 at the upstream boundary at  $x = 30 R_E$  (GSM coordinates are used throughout this study). In  
137 fact, the solar wind boundary conditions are only imposed at the upstream boundary; super-  
138 sonic outflow conditions are used along the rear boundaries and ballistic propagation on the  
139 side boundaries. The solar wind input conditions propagate as 2D planar fronts, from the up-  
140 stream boundary to the magnetosphere. The input conditions can be either real solar wind data  
141 taken from satellite measurements (e.g. ACE or WIND) or idealized configurations. The LFM  
142 simulations presented in this study are driven by idealized solar wind input conditions with the  
143 solar wind variations traveling in the negative  $x$ -direction as  $yz$ -planar fronts. The dipole tilt  
144 of the geomagnetic field is neglected so the SM and GSM coordinate systems are the same in  
145 this study. The propagation of the solar wind as planar fronts and the zero dipole tilt angle both  
146 affect the field line resonance mode structure in the simulation magnetosphere.

147 For the inner boundary condition, the magnetospheric portion of the LFM simulation couples  
148 to a 2D electrostatic model of the ionosphere [Fedder *et al.*, 1995]. Within this model, the elec-  
149 tric potential is obtained from Poisson's equation. The potential is then mapped along dipole  
150 field lines back to the inner boundary of the LFM simulation, which is located at a geocentric  
151 distance of roughly  $2 R_E$ . At the LFM inner boundary, the mapped ionospheric potential is used  
152 to calculate the electric field, which serves as part of the boundary condition for the magneto-  
153 spheric portion of the LFM. The ionospheric conductance, needed for the potential solver, is  
154 specified by an empirical extreme ultraviolet (EUV) conductance model and by a contribution  
155 from particle precipitation. The EUV conductance model, similar to the one used in the AMIE  
156 model [Richmond, 1992], is parametrized by the solar EUV flux. Within the LFM code, the  
157 solar 10.7 cm flux is used to regulate the solar EUV flux and is specified as an input to the  
158 ionospheric model. In the idealized LFM simulations presented in this work, the choice for the

159 10.7 cm flux is somewhat arbitrary and we choose a value of  $100 \times 10^{-22}$  J/m<sup>2</sup> to represent a  
 160 ‘typical’ value. Within the ionospheric model, the EUV conductance is also modified by elec-  
 161 tron precipitation from the magnetosphere, with properties derived from the MHD variables at  
 162 the LFM inner boundary. This entire computation results in a two-way coupling between the  
 163 ionospheric model and the magnetospheric portion of the code, as described in greater detail by  
 164 *Wiltberger et al.* [2009].

## 2.1. Simulation Details

We present results from four LFM simulations: three driven by monochromatic ULF fluctua-  
 tions in the solar wind dynamic pressure and one driven by a continuum of ULF frequencies in  
 the upstream solar wind dynamic pressure fluctuations. Solar wind dynamic pressure (hence-  
 forth,  $p_{dyn}$ ) is not an explicit input in the LFM simulation and we choose to introduce the  $p_{dyn}$   
 fluctuations via the upstream number density, as opposed to the velocity ( $p_{dyn} \propto nv^2$ ). So-  
 lar wind observations typically show that  $p_{dyn}$  variations are carried by the solar wind number  
 density rather than the velocity [e.g. *Kepko and Spence, 2003; Han et al., 2007*]. For the three  
 monochromatic simulations, we impose a number density time series,  $n(t)$ , at the LFM up-  
 stream boundary at  $x = 30 R_E$  of the form:

$$n(t) = n_0 + \delta n \sin(\omega t)$$

165 Here,  $\omega = 2\pi f$  is the monochromatic driving frequency,  $n_0 = 5$  particles/cm<sup>3</sup> is the background  
 166 number density, and  $\delta n$  is amplitude of the perturbation. The three monochromatic driving  
 167 frequencies chosen for analysis in this study are 10, 15, and 25 mHz. In the 10 mHz and 15  
 168 mHz simulations,  $\delta n = 1$  (20% oscillation amplitude) while in the 25 mHz simulation,  $\delta n = 2$   
 169 (40% oscillation amplitude). The larger oscillation amplitude for the input time series in the

170 25 mHz simulation is used to combat the effects of a numerical attenuation/filtering of higher  
 171 frequency components in the LFM simulation. This complication is discussed in greater detail  
 172 in the next subsection.

In the fourth simulation, we impose a continuum of ULF frequencies in the input number density time series:

$$n(t) = n_0 + 0.05 \sum_j \sin(\omega_j t + \phi_j) \quad (1)$$

173 Here, we define  $\omega_j = 2\pi f_j = 2\pi j/10000$  and carry out the summation from  $j = 0, 1, \dots, 500$ .  
 174 This choice defines an input time series with a spectrum that contains a superposition of dis-  
 175 crete frequency fluctuations in the 0 to 50 mHz band and a 0.1 mHz spacing between spectral  
 176 components. We also add a random phase,  $\phi_j$ , to each spectral component. The value of 0.05 in  
 177 the above equation is chosen so that the root-mean square (*RMS*) amplitude of the continuum  
 178 input number density time series is roughly equal to that of the monochromatic input number  
 179 density time series (with 20% oscillation amplitudes). In addition, in all four simulations, we in-  
 180 troduce an appropriate out of phase oscillation in the input sound speed time series, so as to hold  
 181 the thermal pressure constant in the upstream solar wind ( $p_{th} \propto nC_s^2$ ). The background sound  
 182 speed upon which the out of phase oscillation is imposed is 40 km/s. The remaining idealized  
 183 solar wind input parameters are the same in all four simulations and held constant during the  
 184 four hour intervals selected for analysis:  $\mathbf{B} = (0,0,5)$  nT and  $\mathbf{v} = (-600,0,0)$  km/s. We will refer  
 185 to the three monochromatic simulations as the “10 mHz,” “15 mHz,” and “25 mHz simulations”  
 186 and to the fourth simulation as the “continuum simulation.” The nature of the driving in the  
 187 continuum simulation is chosen to examine the magnetospheric response to fluctuations over a  
 188 range of ULF frequencies. Although the input spectrum is not a true continuum, it represents a

189 quasi-broadband driving spectrum derived from quasi-random fluctuations and is sufficient for  
 190 the purposes of this study.

191 In the four simulations presented in this study, an interval of preconditioning is run prior to  
 192 the four hour periods selected for analysis. The simulations begin with one hour of constant  
 193 southward interplanetary magnetic field (IMF) of  $-5$  nT, followed by one hour of constant  
 194 northward IMF ( $B_z = +5$  nT), followed by two hours of constant southward IMF ( $B_z = -5$   
 195 nT), followed by one hour of constant northward IMF ( $B_z = +5$  nT). During this initial five  
 196 hour preconditioning phase, all of the remaining solar wind parameters are held constant, in-  
 197 cluding the number density and sound speed ( $n(t) = 5$  particles/cm<sup>3</sup> and  $C_s(t) = 40$  km/s). The  
 198 oscillations in  $n(t)$  and  $C_s(t)$  described above begin at the end of the five hour preconditioning  
 199 period. In our analyses, we do not wish to include the initial response of the magnetosphere to  
 200 the ‘turning-on’ of the solar wind fluctuations. Thus, we examine the four hours of simulation  
 201 time after the first hour of upstream fluctuations. In summary, the entire duration of the simula-  
 202 tions is 10 hours: hours 0-5 are the preconditioning phase, hours 5-10 are the upstream driving  
 203 phase and the periods selected for analysis are from hours 6-10.

## 2.2. Simulation Caveats

204 Several numerical techniques used in the LFM model influence the simulated wave dynamics  
 205 considered here. These techniques are briefly discussed to facilitate later interpretations. As  
 206 alluded to above, the oscillation amplitudes of the higher frequency  $p_{dyn}$  fluctuations imposed  
 207 at the upstream boundary are attenuated in the simulations. We illustrate this phenomenon in the  
 208 continuum simulation, though a similar effect is encountered in the monochromatic simulations.  
 209 The two panels on the left in Figure 2 show time series of the solar wind  $p_{dyn}$  imposed at the  
 210 upstream boundary at  $(30,0,0) R_E$  (top panel) and at  $(20,0,0) R_E$  in the upstream solar wind in

211 the simulation (bottom panel). Solar wind  $p_{dyn}$  is shown on the vertical scales in both panels  
 212 and ranges from 0 to 5 nPa. Simulation time is shown in hours on the horizontal scale in both  
 213 panels and ranges from 6.0 to 6.5 hrs (decimal time). The time series plotted in the top panel is  
 214 that derived from Equation (1) wherein  $p_{dyn} = m_i n(t) v_{sw}^2$ . Comparison of the two time series  
 215 shows that the higher frequency spectral components imposed at the upstream boundary are  
 216 attenuated downstream from the boundary. In the right panel in Figure 2, the power spectral  
 217 densities ( $PSD$ ) of the full four hour  $p_{dyn}$  time series are shown in blue (at  $(30,0,0) R_E$ ) and  
 218 in green (at  $(20,0,0) R_E$ ). The blue trace shows the relatively uniform distribution of wave  
 219 power across the entire 0 to 50 mHz spectral band, as expected from the Fourier transform of  
 220 Equation (1). Comparison of the two traces shows that the spectral profile input at the upstream  
 221 boundary is significantly altered by the time the fluctuations reach  $(20,0,0) R_E$  in the upstream  
 222 solar wind. For frequencies in the 0 to 10 mHz range, little to no modification of the input  
 223 spectrum is evident. For frequencies in the 10 to 35 mHz range, the oscillation amplitudes in  
 224 the input spectrum are significantly attenuated. For frequencies in the 35 to 50 mHz range, the  
 225 oscillations imposed at the upstream boundary are almost completely suppressed (attenuated)  
 226 in the downstream region.

227 The attenuation of the higher frequency components imposed at the upstream boundary re-  
 228 sults from the numerics in the LFM simulation. The LFM uses nonlinear, total variation di-  
 229 minishing (TVD) switches to allow shock capturing. These switches also cause dissipation as  
 230 the wavelength of a wave approaches the grid scale. Linear dispersion studies with the LFM  
 231 show that this effect becomes significant when a full wavelength is resolved by about 6 grid  
 232 cells or less. For the grid used in these studies, this condition corresponds to  $\approx 3 R_E$  in the  
 233 upstream solar wind and a temporal frequency of  $\approx 30$  mHz. The estimate from Figure 2 shows

234 that the damping rate at 30 mHz is approximately half of the real part of  $\omega$ . This attenuation  
 235 is somewhat higher than what is seen from the dispersion of linear waves. The discrepancy is  
 236 not large and can be explained by two factors. The waves introduced are already nonlinear, will  
 237 tend to self-steepen, and cause the TVD switches to turn on. In addition, the upwind boundary  
 238 condition does not attempt to create a solution accurate to the underlying eighth-order accuracy  
 239 of the LFM transport. The damping rate of the LFM switches depends on the accuracy of the so-  
 240 lution outside of discontinuous regions. The more accurate the solution, the lower the effective  
 241 damping rate is. Nonetheless, the spectral profile that drives the magnetosphere (Figure 2, green  
 242 trace), contains a continuum of ULF frequencies in the  $\approx 0$ -25 mHz range and is sufficient for  
 243 the purposes of this study. We emphasize that the magnetosphere is driven by a continuum of  
 244 ULF frequencies in the upstream  $p_{dyn}$  fluctuations. Later, we will see that the magnetospheric  
 245 response selects particular frequencies from this continuum of upstream fluctuations.

246 The attenuation of the amplitudes in the input time series in the continuum simulation re-  
 247 sults in *RMS* upstream driving at  $(20,0,0) R_E$  on the order of 13%, reduced from the roughly  
 248 20% value imposed at the upstream boundary (in the *RMS* sense described above). As noted  
 249 above, the filtering/attenuation is also encountered in the monochromatic simulations. In the 15  
 250 mHz simulation, the 20% oscillation amplitude imposed at the upstream boundary is reduced  
 251 to roughly 18% at  $(20,0,0) R_E$  in the upstream solar wind. In the 25 mHz simulation, the 40%  
 252 oscillation amplitude imposed at the upstream boundary is reduced to roughly 16% at  $(20,0,0)$   
 253  $R_E$ . As the blue and green traces in Figure 2 suggest, the input oscillation amplitude in the  
 254 10 mHz simulation is not significantly attenuated and remains at roughly 20% at  $(20,0,0) R_E$ .  
 255 Finally, we note that upstream  $p_{dyn}$  driving with amplitudes in the 13-20% range is reasonable

256 when compared with the observational studies discussed in Section 1 and is at the lower end of  
 257 what has been reported.

258 The LFM simulation also does not contain a plasmaspheric model. This simplification leads  
 259 to plasma densities in the simulation inner magnetosphere ( $r < 6.6 R_E$ ) that are lower than  
 260 are typically observed in the real magnetosphere. For example, a nominal value for the number  
 261 density near (5,0,0)  $R_E$  in these LFM simulations is 1.0 particle/cm<sup>3</sup>. Using  $B = 250$  nT, the  
 262 Alfvén speed is then roughly 5,000 km/s in this region, which is larger than in the real inner  
 263 magnetosphere, where 1,000 km/s is a more typical value. A related issue is the use of the  
 264 “Boris correction” [Boris, 1970] in the LFM simulation (see also Lyon *et al.* [2004]). The Boris  
 265 correction includes the perpendicular component of the displacement current in the  $\mathbf{J} \times \mathbf{B}$  force  
 266 of the MHD momentum equation, but with an artificially low speed of light, designated as  $c_A$ .  
 267 The Alfvén wave phase speed is then given as:  $v_{ph} = v_A(1 + v_A^2/c_A^2)^{-\frac{1}{2}} \approx c_A$  when  $v_A \gg c_A$ .  
 268 Here,  $v_A$  is the Alfvén speed,  $v_A = B/\sqrt{\mu_0\rho}$ , where  $B$  is the strength of the magnetic field,  $\rho$  is  
 269 the mass density and  $\mu_0$  is the permeability of free space. The artificial speed of light,  $c_A$ , used  
 270 in these simulations is set to 5,500 km/s for computational efficiency. The propagation speed  
 271 of Alfvén waves is thus limited to  $c_A$  in portions of the dayside magnetosphere. In these LFM  
 272 simulations, roughly 75% of the dayside magnetosphere is unaffected by the use of the Boris  
 273 correction, in terms of closed flux volume. It is only in regions of space where the spherical polar  
 274 coordinate radius is less than  $\approx 5 R_E$  that the propagation speed of Alfvén waves is limited to  
 275  $c_A$ . We also note that if the plasma pressure plays a significant role, fast mode waves can exceed  
 276 this speed and the code remains stable. These issues will be important later when we compute  
 277 the eigenfrequencies of individual field lines in the LFM simulation magnetosphere.

### 3. Simulation Results

We begin by defining a quantity that will be used extensively, the *root-integrated power* (*RIP*) for a given time series:

$$RIP = \left[ \int_{f_a}^{f_b} P(f) df \right]^{1/2}$$

278 Here,  $P(f)$  is the power spectral density of a given time series and the integration is carried  
 279 out over a given frequency band of interest,  $[f_a, f_b]$ . Throughout this work, we compute power  
 280 spectral densities via the multi-taper method [Thomson, 1982; Percival and Walden, 1993],  
 281 which is essentially a windowed, averaged discrete Fourier transform spectral estimator [e.g.  
 282 Press et al., 1992]. For our spectral analyses, the only data manipulation performed on the time  
 283 series prior to the *PSD* computation is a subtraction of the four-hour mean. Note that root-  
 284 integrated power is a measure of the oscillation amplitude in the frequency band,  $[f_a, f_b]$ . For  
 285 example, Parseval's theorem states that the *RMS* amplitude of a given time series is equal to  
 286 the *RIP* when integrated over the entire frequency band  $[0, f_{Ny}]$ , where  $f_{Ny} = 1/2dt$  is the  
 287 Nyquist frequency and  $dt$  is the time sampling rate. The Nyquist frequency in the 10 mHz and  
 288 15 mHz simulations is 16.67 mHz; in the 25 mHz and continuum simulations, it is 50 mHz.  
 289 Finally, note that if the units of the time series are nT, then the units of  $P(f)$  are nT<sup>2</sup>/Hz so that  
 290 the units of *RIP* are nT.

291 Figure 3a shows the equatorial plane distribution of 10 mHz oscillations in the radial elec-  
 292 tric field driven by the monochromatic  $p_{dyn}$  fluctuations (10 mHz simulation). Throughout  
 293 this work, we analyze field components in cylindrical polar coordinates,  $(r, \varphi, z)$  [e.g. Radoski,  
 294 1974; Hughes, 1994]. Root-integrated power (*RIP*) is shown on the color scale and is inte-  
 295 grated over the *driving band*, which we define as a 1 mHz frequency band centered on the  
 296 driving frequency. Thus, for the 10 mHz simulation, the driving band is [9.5,10.5] mHz. The



297 panel shows a GSM equatorial plane cut of the driving band  $RIP$  and the black contour is a  
 298 snapshot of the magnetopause, determined by a field line tracing algorithm [Wiltberger *et al.*,  
 299 2005]. The  $x$  and  $y$  axes are shown in black with  $5 R_E$  spaced tick marks and the sun is to the  
 300 right. The black disk at the origin is the LFM inner boundary, located at  $2.2 R_E$ . Note that the  
 301 bow shock is resolved as the transition from positive wave power in the magnetosheath to zero  
 302 wave power in the solar wind. The bow shock intersects the  $x$ -axis at roughly  $12 R_E$  and the  
 303 magnetopause intersects at roughly  $9 R_E$ . In Figure 3a we see a strong amplitude oscillation in  
 304  $E_r$  along  $r \approx 7 R_E$  on the dayside. Note that the  $E_r$  oscillation amplitude along  $r \approx 7 R_E$  is es-  
 305 sentially zero at the noon meridian. These features in  $E_r$ , shown here in the 10 mHz simulation,  
 306 will be identified as the signature of a toroidal mode field line resonance.

Field line tracing algorithms for the LFM simulation [Wiltberger *et al.*, 2005] allow us to  
 extract Alfvén speed profiles along closed geomagnetic field lines in the simulations. From  
 these Alfvén speed profiles, we can compute estimates to the natural oscillation frequency for  
 a given field line. For example, the WKB estimate to the field line eigenfrequency is given by  
 [Radoski, 1966]:

$$f_n = n \left[ 2 \int_S^N \frac{ds}{v_A(s)} \right]^{-1} \quad \text{for } n = 1, 2, 3, \dots \quad (2)$$

307 Here,  $n$  is the harmonic number of the FLR,  $s$  is the arc length along the field line, and the  
 308 integration is carried out from the southern field line foot point ( $S$ ) to the northern foot point  
 309 ( $N$ ). This estimate to the field line eigenfrequency is essentially the inverse of the travel time  
 310 for an Alfvén wave propagating along the magnetic field line to bounce off the reflecting iono-  
 311 spheres and return to its starting point [Radoski, 1966; Warner and Orr, 1979]. It is a good  
 312 approximation for the higher harmonics (large  $n$ ) and predicts a value about 20% higher than  
 313 the actual fundamental mode eigenfrequency [Takahashi and McPherron, 1984]. The factor

314 of 2 in the above equation is due to the aforementioned ‘bouncing’ and due to the perfectly  
 315 conducting ionospheric boundary condition assumed in FLR theory (e.g. Section 1). While the  
 316 LFM ionospheric boundary condition described in Section 2 results in finite conductivities in  
 317 the model ionosphere, the ionospheric conductivities are large enough that comparisons with  
 318 perfect conductor FLR theory are appropriate [e.g. *Southwood and Hughes*, 1983]. A typical  
 319 value for the dayside Pedersen conductivity in the LFM model ionosphere is 5 Siemens.

320 As noted above, the WKB approximation gives a somewhat crude estimate to the fundamen-  
 321 tal field line eigenfrequency. Thus, we use an alternative method to estimate the local field  
 322 line eigenfrequencies in the LFM simulation. The toroidal mode Alfvén wave eigenfrequen-  
 323 cies are obtained using the toroidal mode Alfvén wave dispersion relation from *Radoski and*  
 324 *Carovillano* [1966] (their equation 25) with a perfect conductor boundary condition at the inner  
 325 radial boundary of the LFM. Since there is some freedom of movement of the boundary (elec-  
 326 tric field mapped from the ionosphere), a more realistic boundary might be lower in altitude  
 327 (leading to a longer field line length), so this boundary condition leads to an upper limit for  
 328 the eigenfrequency. The equation given by *Radoski and Carovillano* [1966] is appropriate for a  
 329 dipole magnetic field, but allows for an arbitrary dependence for the Alfvén speed. For a given  
 330 Alfvén speed profile along an LFM field line (which is non-dipolar), we solve their equation  
 331 using a dipole field line of the same length. For closed LFM field lines on the dayside, the field  
 332 line equatorial radius is typically 5–10% smaller than the dipole field line of the same length.  
 333 This deviation from a dipole geometry is due to the compression of the LFM magnetosphere  
 334 on the dayside. Since the Alfvén speed profile includes the magnitude of the magnetic field,  
 335 the approximation that the field line is dipolar for the wave solution is only in error because of  
 336 the scale factor associated with toroidal motion,  $h_\varphi \propto r$ . Examination of the wave equation

337 of *Singer et al.* [1981], which allows for arbitrary  $h_\varphi$ , shows that our approximation using the  
 338 equation of *Radoski and Carovillano* [1966] (with larger  $h_\varphi$  than is realistic for the LFM field  
 339 line) also leads to an upper limit for the eigenfrequency. As we will see, this alternative esti-  
 340 mate to the FLR eigenfrequency predicts eigenfrequencies closer to the simulated oscillation  
 341 frequencies in the LFM magnetosphere when compared with the WKB estimate. From here on,  
 342 we will refer to this alternative estimate as the ‘dipole estimate.’

343 The solid trace in Figure 4 shows the Alfvén speed profile along the field line that intersects  
 344 the equatorial plane at  $(x, y, z) = (5.0, 5.0, 0)$ , in the 10 mHz simulation. In the  $E_r$  panel in Fig-  
 345 ure 3a, this field line intersects the center of the region of enhanced wave power in the afternoon  
 346 sector. In cylindrical coordinates, the location that this field line intersects the equatorial plane  
 347 is  $(r, \varphi, z) = (7.1, 45^\circ, 0)$ . In Figure 4, Alfvén speed is plotted on the vertical scale from 0 to  
 348 90,000 km/s and distance along the field line,  $s$ , is plotted along the horizontal scale from  $-8.1$   
 349 to  $8.1 R_E$ . The equatorial plane is located at  $s = 0$  and  $s > 0$  is defined to be the northern hemi-  
 350 sphere. Note that the Alfvén speed is a minimum in the equatorial plane and increases towards  
 351 the field line foot points, due to the increasing strength of the magnetic field. It is important  
 352 to remember that closed geomagnetic field lines in the LFM simulation domain have their foot  
 353 points at the inner boundary of the simulation (a spherical shell of radius  $\approx 2 R_E$ ). The dashed  
 354 line in the figure marks the value of 5,500 km/s, which is the Boris corrected speed of light value  
 355 in these LFM simulations. As the figure shows, the local Alfvén speed is less than the Boris cor-  
 356 rected value within the vicinity of the equatorial plane. Moreover, the local Alfvén speed only  
 357 exceeds the Boris corrected value near the ionosphere where the magnetic field strength is very  
 358 large. As noted above, a significant portion of the LFM dayside magnetosphere is not affected  
 359 by the Boris correction and Alfvén waves are able to develop and propagate naturally through

360 these regions. For the field line under consideration in Figure 4, we compute a fundamental  
 361 eigenfrequency of  $f_1 = 11.7$  mHz using the dipole estimate. The WKB estimate (Equation (2))  
 362 gives  $f_1 = 15.3$  mHz, significantly larger than both the dipole estimate and the actual frequency  
 363 of oscillation in  $E_r$  at this location, 10 mHz (e.g. Figure 3a). The reasonable agreement between  
 364 the dipole estimate eigenfrequency and the oscillation frequency suggests that the oscillation in  
 365  $E_r$  is the signature of the fundamental mode FLR. As we will see below, the mode structure  
 366 along the field line supports this claim. Note that the dipole estimate is larger than the simu-  
 367 lated frequency of oscillation, which is consistent with our reasoning above that this estimate  
 368 provides an upper bound.

369 Figure 3 shows a summary of results from the 10 mHz monochromatic simulation. A sim-  
 370 ilar format will be used in subsequent figures to show summaries of the 15 mHz and 25 mHz  
 371 simulation results. As described above, Figure 3a shows  $E_r$  driving band *RIP* in the equatorial  
 372 plane. Figure 3b shows  $E_r$  driving band *RIP* in the 15 LT (i.e.  $\varphi = 45^\circ$ ) meridional plane. The  
 373 black vertical axis is the  $z$ -axis and the horizontal axis lies in the equatorial plane and measures  
 374 radial distance along the 15 LT meridian. The tick marks are spaced at  $5 R_E$  on both axes. In  
 375 Figure 3b, the white trace is the geomagnetic field line that intersects the equatorial plane at  
 376  $r = 7.1 R_E$  on the 15 LT meridian. This same field line was used above to compute the local  
 377 FLR eigenfrequency at  $(r, \varphi, z) = (7.1, 45^\circ, 0)$ . The black trace in the panel is the last closed  
 378 field line in the 15 LT meridional plane. Figure 3b shows that the region of enhanced  $E_r$  wave  
 379 power in the afternoon LT sector of the equatorial plane (e.g. Figure 3a) also extends out of the  
 380 equatorial plane  $\approx 2-3 R_E$  in the positive and negative  $z$ -directions. The region of enhanced  $E_r$   
 381 wave power in the morning LT sector of the equatorial plane exhibits a similar structure out of  
 382 the equatorial plane, though not shown here. The color scales in Figure 3a and Figure 3b are

383 the same and range from 0 to 5 mV/m. In Figure 3c, we plot  $B_\varphi$  driving band  $RIP$  in the 15  
 384 LT meridional plane, i.e. the same plane as Figure 3b.  $B_\varphi$  exhibits maxima at the low-altitude  
 385 (ionospheric) ends of the field line and a node at the equator, as would be expected for a fun-  
 386 damental mode FLR. The last closed field line in the 15 LT meridional plane is again shown in  
 387 black in Figure 3b. The same field line from Figure 3b is shown in white and from here on we  
 388 will refer to this field line as “field line A” in the 10 mHz simulation. Table 1 lists the location  
 389 where field line A in the 10 mHz simulation intersects the equatorial plane, in both Cartesian  
 390 and cylindrical polar coordinates.

391 Figure 3d shows the  $E_r$  power spectral density along the 15 LT meridian in the 10 mHz  
 392 simulation. Radial distance along 15 LT is plotted on the horizontal scale from 2.2 to 10.5  $R_E$   
 393 and frequency is plotted on the vertical scale from 0 to 16.5 mHz.  $E_r$  power spectral density  
 394 ( $PSD$ ) is plotted on the color scale from 0 to 80,000 (mV/m)<sup>2</sup>/Hz. The white shaded region near  
 395  $r = 10 R_E$  represents the approximate location of the magnetopause during the four hours of  
 396 simulation time. The solar wind dynamic pressure fluctuations result in magnetopause motion  
 397 and this motion is represented by the extent of the shaded region. We note that the grid resolution  
 398 here is sufficient to resolve this motion, with the motion occurring across roughly 2-3 grid cells.  
 399 The white dashed traces in the plot show the radial FLR eigenfrequency profiles derived from  
 400 the dipole estimate described above. These four dashed traces correspond to the fundamental  
 401 mode ( $n = 1$ ) and the second through fourth harmonics ( $n = 2, 3,$  and  $4$ ). We also show the  $n$   
 402  $= 1$  profile given by the WKB estimate (solid trace). Note that the WKB estimate is roughly  
 403 20% larger than the dipole estimate, which is consistent with the aforementioned studies [e.g.  
 404 *Takahashi and McPherron, 1984*]. Finally, in Figure 3e, we show driving band  $RIP$  profiles  
 405 along field line A, for  $E_r$  (solid blue trace) and  $B_\varphi$  (solid green trace). Distance,  $s$ , along field

406 line A is shown on the horizontal scale and ranges from  $-8.1$  to  $8.1 R_E$ . The equatorial plane  
 407 is located at  $s = 0$  and  $s > 0$  is defined to be the northern hemisphere.  $E_r$  driving band  $RIP$  is  
 408 shown on the left vertical scale and ranges from 0 to 6.5 mV/m;  $B_\varphi$  driving band  $RIP$  is shown  
 409 on the right vertical scale and ranges from 0 to 9 nT. Note that these  $RIP$  profiles are extracted  
 410 along the white field line in Figure 3b and Figure 3c and can be compared with those two panels  
 411 for consistency. The dashed traces in panel e) and the relevant features in panels a)-e) will be  
 412 discussed in detail in Section 4.

413 Figure 5 and Figure 6 show a summary of results from the 15 mHz and 25 mHz monochro-  
 414 matic simulations, respectively. A similar format to Figure 3 is used. The main difference is  
 415 that in the 15 mHz simulation, we consider the  $RIP$  profiles along two field lines, as opposed  
 416 to just one in the 10 mHz simulation. The locations where these two field lines intersect the  
 417 equatorial plane are shown in Table 1 and the two field lines are traced in white in Figure 5b and  
 418 Figure 5c. In the 25 mHz simulation, we again consider the  $RIP$  profiles along two field lines.  
 419 The locations where these two field lines intersect the equatorial plane are shown in Table 1  
 420 and the two field lines are traced in white in Figure 6b and Figure 6c. For the 15 mHz and 25  
 421 mHz simulations, the  $RIP$  plotted in the respective figures is integrated over the driving band.  
 422 The driving band in the 15 mHz simulation is 14.5-15.5 mHz and, in the 25 mHz simulation, is  
 423 24.5-25.5 mHz.

424 Figure 7 shows the radial profile of  $E_r$   $PSD$  plotted along the 15 LT meridian in the contin-  
 425 uum simulation. The dipole estimate to the FLR eigenfrequency profiles are overlaid in white  
 426 dashed traces and the  $n = 1$  WKB estimate is again shown for comparison (solid white trace).  
 427 We note that there is no driving band in the continuum simulation as the upstream driving con-  
 428 tains a continuum of ULF fluctuations in the 0-25 mHz band. However, a particular frequency

429 can be chosen and qualitatively similar plots to the monochromatic simulation results can be  
 430 produced. For example, to consider fluctuations at 10 mHz in the continuum simulation, we  
 431 could plot  $RIP$  integrated over [9.5,10.5] mHz. These plots reveal qualitatively similar features  
 432 to the 10 mHz monochromatic simulation results in Figure 3a-c (not shown here). Similarly,  
 433 profiles of  $E_r$  and  $B_\varphi RIP$  (integrated over [9.5,10.5] mHz) along a field line that intersects the  
 434 equatorial plane in the continuum simulation at  $(r, \varphi, z) = (7.1, 45^\circ, 0)$  look qualitatively similar  
 435 to the profiles shown in Figure 3e (not shown here).

#### 4. Discussion

436 We now provide a detailed discussion of the simulation results presented in the previous  
 437 section. In Section 4.1, we interpret the simulation results as the signatures of toroidal mode  
 438 field line resonances. In Section 4.2, we show that the simulated toroidal mode FLRs exhibit  
 439 polarization signatures similar to those seen in observations. Finally, in Section 4.3, we briefly  
 440 consider the Poynting vector and discuss the relevant mechanisms for energy dissipation in the  
 441 system.

##### 4.1. Evidence of Field Line Resonances

442 We begin by considering the results from the 10 mHz monochromatic simulation, shown in  
 443 Figure 3. We interpret the oscillations in  $E_r$  and  $B_\varphi$  on the dayside as signatures of toroidal  
 444 mode field line resonances. As discussed in Section 1, the dominant oscillating field com-  
 445 ponents for a toroidal mode FLR are expected to be  $E_r$  and  $B_\varphi$  in the approximate dipolar  
 446 geometry of the dayside simulation region. We note here that the ‘poloidal mode’ and ‘toroidal  
 447 mode’ terminology is strictly valid only for an axisymmetric, dipole magnetosphere. Portions  
 448 of the real magnetosphere are certainly non-dipolar, particularly the nightside and the magneto-

449 tail. Similarly, the LFM magnetosphere deviates from a dipolar configuration on the nightside  
 450 [Lyon *et al.*, 2004]. However, in the dayside LFM inner magnetosphere ( $r < 10 R_E$ ) in these  
 451 simulations, the geometry is roughly dipolar. We have confirmed this feature of the simulated  
 452 magnetosphere by comparing contours of constant magnetic field in the equatorial plane with  
 453 circles and finding good agreement between the two on the dayside, within a tolerance of 0.5  
 454  $R_E$ . Thus, we use the terminology ‘toroidal mode’ without hesitation and assume that oscilla-  
 455 tions in the  $B_\varphi$  and  $E_r$  LFM field components are an accurate representation of a toroidal mode  
 456 oscillation on the dayside.

457 Returning to the 10 mHz simulation results, the radial profile of  $E_r$  wave power along the  
 458 15 LT meridian, shown in Figure 3d, reveals an enhancement in 10 mHz wave power near  $r =$   
 459  $7.1 R_E$ . The radial profile of the fundamental mode field line eigenfrequency ( $n = 1$ , dashed  
 460 line) intersects this region of enhanced wave power. This suggests that the 10 mHz oscillation  
 461 in  $E_r$  near  $r = 7.1 R_E$  on the 15 LT meridian is the signature of the fundamental toroidal  
 462 mode FLR. The profiles of  $E_r$  and  $B_\varphi$  RIP along field line A (Figure 3e), which intersects  
 463 the 15 LT meridian at  $r = 7.1 R_E$ , support this conclusion. The standing wave schematics for  
 464 the fundamental mode FLR, shown in Figure 1, indicate that in the equatorial plane, the electric  
 465 field has an antinode and the magnetic field has a node. This structure of the field line oscillation  
 466 amplitude profiles is evident in Figure 3e. Out of the equatorial plane along the field line, the  $B_\varphi$   
 467 oscillation amplitude (solid green) increases towards the field line foot points at the simulation  
 468 inner boundary. This profile is consistent with the  $n = 1$  schematic shown in Figure 1, where  
 469 the magnetic field has antinodes at the field line foot points. In addition, the amplitude of the  
 470 oscillation in  $E_r$  (solid blue trace in Figure 3e) decreases monotonically following the field



471 line away from the equator until nodes are reached near  $s = \pm 4.5 R_E$ . These two nodes are  
 472 consistent with an  $n = 1$  FLR, though this is not obvious when comparing with Figure 1.

473 The additional nodes in the  $E_r$  profiles are due to the coordinate system chosen for analysis,  
 474 the curvature of the magnetic field lines and the effect of scale factors. Field line curvature  
 475 ensures that the scale factors perpendicular to the magnetic field are not unity and change along  
 476 the field line. In dipole coordinates, the perpendicular scale factor,  $h_r$ , multiplied by the per-  
 477 pendicular electric field,  $E_r$ , has a discrete harmonic solution along the field [Allan and Knox,  
 478 1979a, b; Ozeke and Mann, 2004]. The choice of cylindrical polar coordinates,  $(r, \varphi, z)$ , also  
 479 plays a role in the additional nodes in  $E_r$ . In this coordinate system, the  $r$ -direction points out-  
 480 ward from the cylindrical (i.e. dipole) axis. Where the magnetic field line crosses the equatorial  
 481 plane, the direction associated with the  $r$ -component is perpendicular to the magnetic field line  
 482 (recall there is no dipole tilt in these simulations). But as one moves out of the equatorial plane  
 483 along field line A (e.g. Figure 3b), a point is reached on the field line where the (cylindrical)  
 484 radial direction is tangent to the magnetic field direction. Thus, in cylindrical polar coordinates,  
 485 there must be a node in  $E_r$  at this location (because  $\mathbf{E} = -\mathbf{v} \times \mathbf{B}$  is always perpendicular to the  
 486 equilibrium magnetic field,  $\mathbf{B}$ ). The schematics shown in Figure 1 do not show these two addi-  
 487 tional nodes in the  $n = 1$  electric field profile because the schematics are drawn for a uniform  
 488 plasma permeated by straight magnetic field lines.

489 To verify that the FLR mode structure profiles reproduced by the LFM simulation are con-  
 490 sistent with FLR theory, we use the same method that was used in Section 3 to compute the  
 491 dipole estimate to the field line eigenfrequency. Here, the theoretical mode structure profiles  
 492 are obtained from the toroidal Alfvén wave equations of Radoski and Carovillano [1966] and  
 493 the fields are projected in cylindrical polar coordinates. Again, we use the Alfvén speed pro-

494 file from the LFM simulation along a dipole field line of the same length as the LFM field  
 495 line. The resulting mode structure profiles for the fundamental toroidal mode FLR are shown  
 496 as dashed traces in Figure 3e for  $B_\varphi$  (green dashed) and  $E_r$  (blue dashed). The theoretical pro-  
 497 files obtained from the dipole dispersion relation show very good agreement with the profiles  
 498 reproduced by the LFM simulation. We emphasize that the schematics shown in Figure 1 are  
 499 the “standard” picture of FLR oscillations often encountered in the literature [e.g. *Southwood*  
 500 *and Hughes*, 1983]. However, we have shown here that the FLR mode structure is dependent  
 501 upon the coordinate system chosen and care must be exercised when comparing simulations  
 502 (and observations) with theory. Field-aligned electric field mode structure profiles plotted in the  
 503  $(\hat{\varphi} \times \mathbf{B}/|\hat{\varphi} \times \mathbf{B}|)$ -direction, where  $\mathbf{B}$  is the equilibrium magnetic field, would not show these  
 504 additional nodes. Note that the  $\varphi$ -variable in cylindrical polar coordinates is the same coordi-  
 505 nate in spherical polar and dipole coordinates. Thus, the  $B_\varphi$  profile shown in Figure 3e will be  
 506 consistent with the schematics shown in Figure 1, which are often envisioned in one of these  
 507 two systems. The simulation results shown in Figure 3 provide convincing evidence to support  
 508 the claim that the  $n = 1$  toroidal mode FLR is excited in the 10 mHz monochromatic simulation.

509 We now turn our attention to the results from the 15 mHz monochromatic simulation, shown  
 510 in Figure 5. The radial profile of  $E_r$  wave power along the 15 LT meridian (Figure 5d) shows a  
 511 strong enhancement in 15 mHz wave power near  $r = 6.5 R_E$  and a secondary, weaker enhance-  
 512 ment near  $r = 9.2 R_E$  (see also Figure 5a and Figure 5b). In Figure 5d, note that the  $n = 1$  field  
 513 line eigenfrequency profile intersects the region of enhanced wave power near  $r = 6.5 R_E$  and  
 514 that the  $n = 3$  profile intersects the enhanced wave power near  $r = 9.2 R_E$ . This interpretation  
 515 suggests that both the  $n = 1$  and  $n = 3$  toroidal mode FLRs are excited in the 15 mHz simulation.  
 516 The field line mode structure profiles shown in Figure 5e and Figure 5f support this conclusion.

517 The  $B_\varphi$  mode structure along field line A (Figure 5e), which intersects the equatorial plane at  $r$   
 518 = 6.5 on the 15 LT meridian, shows a node in the equatorial plane and antinodes near the field  
 519 line foot points. This mode structure is consistent with the  $n = 1$  schematic for the magnetic  
 520 field shown in Figure 1. In addition, the  $E_r$  mode structure along field line A shows an antinode  
 521 in the equatorial plane, nodes at the field line foot points, and two additional nodes near  $s =$   
 522  $\pm 4 R_E$ . As was the case for the 10 mHz simulation, this  $E_r$  profile is consistent with an  $n =$   
 523 1 toroidal mode FLR, when considered in cylindrical polar coordinates and the effects due to  
 524 scale factors are considered (e.g. Figure 3e). Thus, the available evidence indicates that the fun-  
 525 damental toroidal mode FLR is excited in the 15 mHz simulation along field lines that intersect  
 526 the equatorial plane near  $r = 6.5 R_E$  on the 15 LT meridian.

527 The  $B_\varphi$  and  $E_r$  mode structure profiles along field line B in the 15 mHz simulation (Figure 5f)  
 528 are consistent with the  $n = 3$  toroidal mode FLR interpretation. The  $B_\varphi$  profile again has a node  
 529 in the equatorial plane but also has two additional nodes near  $s = \pm 8 R_E$  along the field line.  
 530 This profile is consistent with the  $n = 3$  schematic for the magnetic field shown in Figure 1,  
 531 where a node occurs in the equatorial plane, with an additional node between the equatorial  
 532 plane and each field line foot point. In addition, the  $E_r$  mode structure along field line B shows  
 533 an antinode in the equatorial plane, nodes at the field line foot points, and additional nodes  
 534 near  $s = \pm 7 R_E$  and  $s = \pm 4 R_E$ . As was the case for the fundamental radial electric field  
 535 oscillation, this mode structure is consistent with an  $n = 3$  toroidal mode FLR, when considered  
 536 in cylindrical polar coordinates and the effects due to scale factors are considered (not shown  
 537 here). Thus, the  $n = 3$  toroidal mode FLR is excited in the 15 mHz simulation along field lines  
 538 that intersect the equatorial plane near  $r = 9.2 R_E$  on the 15 LT meridian. Finally, we note  
 539 that there are very faint features near 3.5 mHz in the  $E_r$  spectrum along the 15 LT meridian

(Figure 5d). These features are most likely due to aliasing [e.g. *Press et al.*, 1992] and are very small amplitude (roughly an order of magnitude less than the 15 mHz oscillations).

We now consider the results from the 25 mHz monochromatic simulation, shown in Figure 6. The radial profile of  $E_r$  wave power along the 15 LT meridian (Figure 6d) shows enhancements in wave power near  $r = 5.8$  and  $8.3 R_E$ . The  $n = 1$  eigenfrequency profile intersects the region of enhanced wave power near  $r = 5.8 R_E$ , which suggests that this feature is the signature of the  $n = 1$  toroidal mode FLR. The  $B_\varphi$  and  $E_r$  mode structure along field line A (Figure 6e) supports this conclusion for the reasons discussed above. Moreover, the  $n = 3$  eigenfrequency profile intersects the region of enhanced wave power near  $r = 8.3 R_E$ , which suggests that this feature is the signature of the  $n = 3$  toroidal mode FLR. Again, the  $B_\varphi$  and  $E_r$  mode structure along field line B (Figure 6f) supports this conclusion. We also note the possible signature of the  $n = 5$  FLR in Figure 6b and Figure 6c, in the region of space between field line B and the last closed field line. Finally, we note that the FLR oscillation amplitudes in the three monochromatic simulations are the strongest in the 10 mHz simulation and the weakest in the 25 mHz simulation. This variation is a result of the filtering/attenuation issue described in Section 2, where the attenuation of the oscillation amplitudes in the upstream dynamic pressure fluctuations becomes more pronounced at higher frequencies.

We now take up the results from the continuum simulation, shown in Figure 7. The radial profile of  $E_r$  wave power along the 15 LT meridian shows remarkable agreement with the FLR eigenfrequency profiles (dashed traces). The  $n = 1$  and  $n = 3$  eigenfrequency traces coincide with the regions of enhanced wave power along the 15 LT meridian. This coincidence suggests that the continuous spectra of  $n = 1$  and  $n = 3$  FLRs are excited in the continuum simulation. Though only shown here at the 15 LT meridian, the  $n = 1$  and  $n = 3$  FLRs are excited across

563 all of the dayside, excluding near the noon meridian, as was the case in the monochromatic  
 564 simulations. Note that the  $n = 2$  and  $n = 4$  eigenfrequency traces lie in between the regions of  
 565 enhanced wave power, suggesting that only odd mode number toroidal mode FLRs are excited  
 566 in the continuum simulation. This effect is easily explained by considering the nature of the  
 567 upstream forcing. As discussed in Section 2, in the LFM simulation the solar wind propagates  
 568 as planar fronts towards the magnetosphere. Furthermore, in these LFM simulations, the solar  
 569 wind velocity has only an  $x$ -component, so that the planar fronts are parallel to the  $yz$ -plane  
 570 and propagate in the negative  $x$ -direction. As these idealized simulations are conducted with  
 571 no dipole tilt, the planar fronts impact the subsolar, equatorial plane of the magnetosphere first,  
 572 which lies on the positive  $x$ -axis. This impact leads to a situation where the forcing is symmetric  
 573 about the equatorial plane, along closed field lines. Consequently, the perturbations in  $E_r$  are  
 574 symmetric and those in  $B_\varphi$  are antisymmetric, with respect to the equatorial plane [Allan *et al.*,  
 575 1985; Lee and Lysak, 1989] and only odd mode number toroidal mode FLRs can be excited.  
 576 We note that a similar situation was reported in the numerical simulations of Lee and Lysak  
 577 [1989, 1991] who modeled FLRs in a dipole geometry with impulsive upstream forcing, which  
 578 was also symmetric about the equatorial plane. Additionally, we note that the absence of the  $n$   
 579  $= 2$  and  $n = 4$  harmonics can be understood by the fact that the overlap integrals to these modes  
 580 are identically zero [e.g. Southwood and Kivelson, 1986; Wright, 1992]. If a slight tilt were  
 581 introduced to the dipole axis, there would be a weak coupling to the  $n = 2$  and  $n = 4$  harmonics.  
 582 The node in  $E_r$  near the noon meridian is also due to the symmetry in the upstream forcing  
 583 and a node in  $\partial B_z / \partial \varphi$ , which is proportional to the linear magnetic pressure gradient in the  
 584 azimuthal direction [Rickard and Wright, 1994, 1995]. In the MHD momentum equation, this  
 585 quantity is responsible for forcing the  $\varphi$ -component, hence the node in  $v_\varphi$  and  $E_r$ . Similarly,

586 the monochromatic simulation results (Figure 3, Figure 5, and Figure 6) do not show any FLRs  
 587 near noon or any even mode number FLR signatures. The monochromatic simulations were  
 588 also conducted with no dipole tilt and driven with planar fronts propagating in the negative  $x$ -  
 589 direction. It is interesting to note that observational studies of FLRs often report that the mode  
 590 structure is statistically odd mode number [e.g. *Anderson et al.*, 1990]. Finally, note that the  
 591 radial profile of  $E_r$  PSD along the 15 LT meridian in the continuum simulation (Figure 7)  
 592 shows that multiple FLR harmonics can be excited on the same field line, which has been  
 593 reported in observations [e.g. *Singer et al.*, 1979].

## 4.2. Polarization Characteristics

594 Observations of ULF pulsations attributed to field line resonances often show an approxi-  
 595 mately  $180^\circ$  phase change radially across a peak in wave power [*Samson et al.*, 1971; *Walker*  
 596 *et al.*, 1979; *Ruohoniemi et al.*, 1991]. This observational signature is predicted by the FLR  
 597 theory [*Chen and Hasegawa*, 1974; *Southwood*, 1974]. The FLRs in the LFM simulation also  
 598 exhibit this signature, as illustrated in Figure 8 for the fundamental mode FLR in the afternoon  
 599 sector in the 10 mHz simulation (e.g. Figure 3a near  $r = 7.1 R_E$ ). The solid trace in Figure 8  
 600 shows the radial profile of the  $E_r$  driving band *RIP* along the 15 LT meridian. Radial distance,  
 601  $r$ , along the 15 LT meridian is shown on the horizontal scale from 5.5 to 8.9  $R_E$ . The  $E_r$  driving  
 602 band *RIP* is shown on the left vertical scale (labeled ‘ $E_r$  amplitude’ in the figure) and ranges  
 603 from 0 to 7 mV/m. The solid trace in Figure 8 can be compared with Figure 3a for consistency.  
 604 The dashed trace in Figure 8 shows the relative phase computed from the  $E_r$  time series along  
 605 15 LT meridian via a fast Fourier transform method. The  $E_r$  time series at the peak in wave  
 606 power serves as the reference time series (i.e. relative phase = 0) and relative phase is plotted  
 607 on the right vertical scale from  $-100$  to  $100$  degrees. From the figure, we see an approximately

180° change in phase radially across the peak in power, i.e. radially across the location of the FLR in the equatorial plane. This signature of the simulated FLR, including the decrease in phase as  $r$  increases, is consistent with both the theory [e.g. *Chen and Hasegawa, 1974*] and the observations [e.g. *Ruohoniemi et al., 1991*] described above. The  $n = 1$  and  $n = 3$  FLRs identified in the 15 mHz and 25 mHz simulations also show phase changes radially across the respective peaks in wave power. We note, however, that the phase change is not always  $\approx 180^\circ$ , as it is for the  $n = 1$  FLR in the 10 mHz simulation. For example, for the  $n = 1$  and  $n = 3$  FLRs in the 15 mHz simulation, the phase changes are in the 160-200° range. In the 25 mHz simulation, the phase changes are on the order of 100°, which is significantly less than the phase change in the 10 mHz simulation. The deviations from the theoretical expectations may be due to the interaction between multiple resonances [*McDiarmid et al., 1999*], as there is only the fundamental resonance in the 10 mHz simulation. Also, as noted above, the continuum simulation does not show a radial peak in wave power along the 15 LT meridian unless power at a particular frequency (from the continuum of FLR frequencies) is considered (e.g. Figure 7). If power at a particular frequency is chosen for analysis, then we find a similar phase reversal across the peak in wave power (not shown here).

Another feature of FLR observations is a change in the sense of polarization across local noon [*Samson et al., 1971; Fukunishi et al., 1975*]. Figure 9 shows hodograms of the electric field near the location of the fundamental mode FLR in the 10 mHz simulation (e.g. Figure 3a near  $r = 7.1 R_E$ ). The left column in the figure shows the electric field hodograms in the equatorial plane in the afternoon sector at  $\mathbf{x} = (5.3, 5.3, 0)$ ; the right column shows the hodograms in the morning sector at  $\mathbf{x} = (5.3, -5.3, 0)$ . The top row shows the hodograms for the Cartesian coordinate electric field components,  $E_x$  and  $E_y$ , where a ‘+’ is plotted at each time step for the entire four hours

631 of simulation time. The bottom row shows the hodograms for the cylindrical polar coordinate  
632 electric field components,  $E_r$  and  $E_\varphi$ . The only data manipulation done on the time series is a  
633 removal of the four-hour mean; the time series are not filtered. Comparing the two hodograms  
634 in the top row, we see that the axis tilt in the electric field polarization has a positive slope in the  
635 afternoon sector and a negative slope in the morning sector. This feature indicates a polarization  
636 reversal in the electric field oscillations across the noon meridian, a result consistent with FLR  
637 observations. The FLR theory of *Chen and Hasegawa* [1974] and *Southwood* [1974] predicts  
638 that the polarization is linear near the peak in wave power, which is clearly evident in Figure 9.  
639 Moreover, the theory also predicts that the polarization is elliptical for  $L$ -shells adjacent to the  
640 resonance, which is also reproduced in the LFM simulation (not shown here). Hodograms of  
641 the electric field components near the morning and afternoon sector locations of the FLRs in the  
642 15 mHz and 25 mHz simulations show similar polarization reversals across local noon.

643 Several authors have noted that the observed polarization reversal across 12 LT can be ex-  
644 plained by assuming that the compressional energy that drives the FLRs originates in Kelvin-  
645 Helmholtz waves near the magnetopause [*Samson et al.*, 1971; *Walker et al.*, 1979; *Southwood*  
646 *and Hughes*, 1983]. However, any disturbance whose origin lies in the solar wind and propa-  
647 gates around the magnetosphere with the solar wind can also produce the observed change in  
648 polarization across local noon [*Hughes*, 1994]. Thus, the observed polarization change does  
649 not necessarily implicate the Kelvin-Helmholtz instability for FLR excitation; it merely impli-  
650 cates the solar wind. Other authors [*Yumoto and Saito*, 1983; *Rostoker and Sullivan*, 1987]  
651 have argued against a Kelvin-Helmholtz mechanism for FLR excitation on a variety of grounds.  
652 The field line resonances in this study are ultimately driven by solar wind dynamic pressure  
653 fluctuations, which results in the polarization reversal across local noon.



### 4.3. Energy Considerations

We now consider the flux of energy near the FLR in the LFM simulation. The energy flux is examined by considering the Poynting vector,  $\mathbf{S}$ :

$$\mathbf{S} = \frac{\mathbf{e} \times \mathbf{b}}{\mu_0}$$

where  $\mathbf{e}$  is the perturbed electric field and  $\mathbf{b}$  is the perturbed magnetic field. The perturbed magnetic field is defined as  $\mathbf{b} = \mathbf{B} - \text{mean}(\mathbf{B})$ , where  $\mathbf{B}$  is the magnetic field and the mean is calculated over the four hours of simulation time (similarly for the perturbed electric field). In fact, a more useful quantity is the time averaged Poynting vector,  $\langle \mathbf{S} \rangle$ :

$$\langle \mathbf{S}(\mathbf{x}) \rangle = \frac{1}{T} \int_0^T \mathbf{S}(\mathbf{x}, t) dt$$

654 where  $T$  is the period of the oscillation. The time averaged Poynting vector gives the net energy  
 655 flux over one period of oscillation, as opposed to the instantaneous direction of energy flux given  
 656 by  $\mathbf{S}$ . As we are considering the Poynting vector, our discussion of energy flow only accounts  
 657 for electromagnetic power, i.e. we do not consider the contributions from the flux of kinetic  
 658 energy or thermal energy [e.g. *Kouznetsov and Lotko, 1995*].

659 Figure 10 shows the parallel component of the time averaged Poynting vector,  $\langle S_{\parallel} \rangle$ , along  
 660 field line A in the 10 mHz simulation. We define a positive (negative) value of  $S_{\parallel}$  as the compo-  
 661 nent of  $\mathbf{S}$  parallel (antiparallel) to  $\mathbf{B}$ . Distance,  $s$ , along field line A is plotted on the horizontal  
 662 scale from  $-8.1$  to  $8.1 R_E$  and  $s > 0$  is defined to be the northern hemisphere. The profile  
 663 of  $\langle S_{\parallel} \rangle$  shows that, near the equatorial plane, a net flow of energy is directed from the equato-  
 664 rial plane towards the northern and southern ionospheres. The direction is consistent with the  
 665 development of a resonant field line oscillation forced at the equatorial plane.

666 In the three monochromatic simulations, the monochromatic fluctuation in the upstream dy-  
667 namic pressure drives compressional waves on the dayside magnetosphere (not shown here).  
668 These compressional waves energize toroidal mode field line resonances at locations where the  
669 frequency of the compressional source matches a local field line eigenfrequency. The open  
670 magnetospheric configuration in the LFM simulation allows for compressional energy to be lost  
671 into the nightside magnetosphere. This geometric configuration is a significant advance over the  
672 closed magnetospheric numerical simulations of the past [e.g. *Lee and Lysak*, 1989, 1991], is a  
673 more realistic representation of the solar wind-magnetosphere-ionosphere system than previous  
674 work in open geometries [*Lee and Lysak*, 1999; *Lee et al.*, 2004], and provides a new tool for  
675 studying resonant oscillations in the magnetosphere.

676 The controlled nature of the LFM numerical experiments described in this work allows us to  
677 probe deeper into the flow of energy through the coupled solar wind-magnetosphere-ionosphere  
678 system. To this end, we ran the four simulations in this study with the upstream dynamic pres-  
679 sure fluctuations turned off after the four hour driving phase. The resonant field line oscillations  
680 die out quickly, within roughly 2-3 wave periods. In the real magnetosphere, ionospheric dis-  
681 sipation may be the primary mechanism for FLR decay [*Newton et al.*, 1978]. However, this  
682 dissipation does not appear to be the limiting mechanism in the version of LFM simulation used  
683 in this study; the simulation results suggest that the rapid decay of the FLRs is due to numer-  
684 ical dissipation. To confirm this assertion, we have conducted several other LFM simulations,  
685 nearly identical to the 10 mHz simulation presented here. In the first set of new simulations,  
686 we changed the solar 10.7 cm flux, which serves as an input to the ionospheric model (see Sec-  
687 tion 2), to  $200 \times 10^{-22} \text{ J/m}^2$  and  $300 \times 10^{-22} \text{ J/m}^2$  (it was  $100 \times 10^{-22} \text{ J/m}^2$  in the 10 mHz monochro-  
688 matic simulation). The increase in solar 10.7 cm flux has the effect of increasing the Pedersen

689 conductivity in the dayside ionosphere from its nominal value of roughly 5 Siemens in the 10  
690 mHz simulation, to a value of roughly 8.5 and 10 Siemens in the two new simulations (near  
691 the foot points of the resonant field lines). The full-width at half maximum (FWHM) of the  
692  $E_r$  amplitude in the equatorial plane, which is governed by the decay rate of the FLR, does not  
693 vary significantly across the three simulations and has a value of roughly  $1.6 R_E$ . As a second  
694 set of tests, we ran the LFM simulation coupled to a simpler ionospheric model, one in which  
695 the Pedersen conductivity is maintained at a constant value [Fedder *et al.*, 1995]. We ran three  
696 simulations in which the upstream driving conditions were identical to the 10 mHz simulation  
697 but where the constant value of the ionospheric Pedersen conductivity was maintained at 5, 10,  
698 and 20 Siemens, respectively. Again, the FWHM of the  $E_r$  amplitude in the equatorial plane  
699 did not vary significantly across the three simulations and had a value of roughly  $1.7 R_E$ . In  
700 either set of tests, the FWHM of the resonant oscillations did not change significantly when the  
701 ionospheric Pedersen conductivity was changed. Thus, in the LFM simulation, the FLR decay  
702 rates, which are related to the FWHM, are not significantly affected by the value of the Pedersen  
703 conductivity in the ionosphere. This result implies that the finite ionospheric conductance is not  
704 the dominant sink of FLR power in the LFM and we suggest that the rapid decay of the FLRs  
705 is primarily through numerical dissipation.

706 Finally, we note that there are roughly six grid cells across the FWHM in these LFM sim-  
707 ulations. If the FLRs are not fully resolved in the radial direction, there can be an unphysical  
708 leakage of wave energy from the FLR into the fast compressional mode [Stellmacher *et al.*,  
709 1997]. Thus, the rapid decay of the FLRs in these simulations may not be entirely due to nu-  
710 merical dissipation. In addition, there could be damping due to the fact that the LFM grid is not  
711 magnetically aligned. In the non-Cartesian, distorted spherical mesh used in the LFM simula-

712 tion [Lyon *et al.*, 2004], resonant field lines thread across grid cells, into neighboring grid cells  
713 that have field lines magnetically connected to different  $L$ -shells. Thus, wave energy from the  
714 resonant  $L$ -shell can leak into neighboring, non-resonant  $L$ -shells. This would also be the case  
715 for other global MHD models, such as BATS-R-US [Gombosi *et al.*, 2003] and OpenGGCM  
716 [Raeder *et al.*, 2001], which both use a Cartesian grid.

717 We acknowledge that the decay rates/FWHMs are probably not a realistic representation of  
718 FLRs in the real magnetosphere. However, the main results of this study are: that FLRs can  
719 be driven by dynamic pressure fluctuations and that the LFM simulation can reproduce FLRs  
720 in a realistic solar wind-magnetosphere-ionosphere geometry with global FLR characteristics  
721 consistent with observations. We emphasize that none of these results depend critically on the  
722 decay rate of the FLRs, as we are continually driving the magnetosphere during the time periods  
723 in which the above results are obtained. The dissipation of energy in the LFM magnetospheric  
724 system warrants a more detailed investigation and this will be the subject of future work. A re-  
725 lated issue is the presence of cavity/waveguide mode oscillations in the LFM simulation and the  
726 nature of the coupling between the FLR and the cavity/waveguide mode. The simulation results  
727 presented here suggest that the LFM is able to reproduce cavity/waveguide mode oscillations  
728 under these driving conditions (see also *Claudepierre et al.* [2009]). Moreover, the open con-  
729 figuration of the LFM magnetosphere allows for the fast mode compressional energy to be lost  
730 downtail and the cavity behaves more like a waveguide [e.g. *Samson et al.*, 1992; *Harrold and*  
731 *Samson*, 1992; *Wright*, 1994; *Rickard and Wright*, 1994]. These issues related to the coupling  
732 of cavity mode/waveguide energy into the FLRs in the LFM simulation will also be the subject  
733 of future work.

## 5. Summary and Conclusions

734 In this work, the Lyon-Fedder-Mobarry (LFM) global, three-dimensional MHD simulation  
735 was used to investigate the role that solar wind dynamic pressure fluctuations play in the gen-  
736 eration of magnetospheric ULF pulsations. The LFM simulations were driven with idealized  
737 solar wind input parameters, where ULF fluctuations were introduced into the time series of  
738 solar wind dynamic pressure. In three of the simulations, a monochromatic sinusoidal variation  
739 in the solar wind dynamic pressure was used to drive the magnetosphere. In these simulations,  
740 the monochromatic fluctuation in the upstream dynamic pressure drove compression of the day-  
741 side magnetosphere. Resulting compressional waves energized toroidal field line resonances at  
742 locations where the frequency of the compressional source, ultimately solar wind pressure os-  
743 cillations, matched a local field line eigenfrequency. In the fourth simulation, a continuum of  
744 ULF frequencies was introduced into the upstream dynamic pressure fluctuations. This configu-  
745 ration served as a quasi-broadband stimulus to the magnetosphere and resulted in the excitation  
746 of a continuous spectrum of toroidal mode field line resonances on the dayside. The simulated  
747 field line resonances also showed several characteristics consistent with observations, including  
748 a phase reversal radially across the location of the resonance, a change in the sense of polar-  
749 ization across the noon meridian, and a net flux of energy out of the equatorial plane into the  
750 ionosphere.

751 The idealized solar wind input parameters used in this study were chosen to represent con-  
752 tinuous driving of the magnetosphere. In contrast with the driving in the continuum simulation,  
753 a discrete feature in the solar wind dynamic pressure could also have been used to drive the  
754 simulation. A step function increase in the solar wind dynamic pressure would provide a true  
755 broadband stimulus to the magnetosphere. We have analyzed results from idealized LFM sim-

756 ulations where a large step function increase in the solar wind dynamic pressure ( $\Delta p/p \sim 5$ )  
757 was used to drive the magnetosphere. The initial results suggest that the broadband stimulus  
758 can drive FLRs on the dayside, though the oscillations die out quickly, within 2-3 wave periods.

759 The majority of the analyses in this study were done on the LFM fields near the 15 LT merid-  
760 ian in the afternoon sector. However, the simulated FLRs are not localized near 15 LT and  
761 extend across the entire dayside, excluding the 12 LT region (e.g. Figure 3a, Figure 5a and  
762 Figure 6a). We also emphasize that the values of the resonant frequencies reported in this study  
763 should not be compared directly with observations. The primary factor controlling the field line  
764 eigenfrequencies in the simulations is the Alfvén speed profile along the field line (the length  
765 of the field line and the ionospheric boundary conditions are the other controlling factors). The  
766 version of the LFM simulation code used in this study does not contain a plasmaspheric model,  
767 which leads to plasma densities in the inner magnetosphere lower than those typically observed  
768 in the real magnetosphere. The low values for the plasma density result in large values of the  
769 Alfvén speed and large FLR eigenfrequency values on the LFM dayside magnetosphere. A  
770 new version of the LFM simulation, with a realistic plasmaspheric model, is currently under  
771 development and will be used in future studies of resonant ULF waves in the LFM.

772 The study of ULF pulsations presented in this work offers a new perspective of resonant ULF  
773 waves, when compared with previous numerical work. The most obvious difference between  
774 this and previous work is the realistic magnetospheric geometry in the LFM simulation. The  
775 numerical studies of *Lee and Lysak* [1989, 1991] and *Allan et al.* [1986] used a dipolar mag-  
776 netospheric model and a hemi-cylindrical magnetospheric model, respectively. Both of these  
777 model magnetospheres were closed and, thus, did not allow for a downtail loss of compres-  
778 sional wave energy into the nightside, which the LFM is able to reproduce in a realistic fashion.

779 To the best of our knowledge, the only other study that has used a random/continuum driver  
780 to excite FLRs is the work of *Wright and Rickard* [1995]. The differences between the *Wright*  
781 *and Rickard* [1995] study and the present study are again likely due to the different geometries  
782 used. Moreover, the realistic interaction of the solar wind with the magnetosphere in the LFM  
783 simulation allows for the natural development of the magnetopause, bow shock, and magne-  
784 tosheath. In addition, in the numerical work of *Lee and Lysak* [1989, 1991] and *Allan et al.*  
785 [1986], a particular value for the azimuthal mode number,  $m$ , must be specified in their models.  
786 In the LFM simulations presented in this work, the azimuthal mode structure of the resonant  
787 oscillations falls out naturally from the model. Spectral analyses of the equatorial plane electric  
788 field components shows that  $m \leq 6$  for the oscillations studied in this work, and that the spectra  
789 are typically peaked in the  $m = 2-4$  range. The azimuthal mode number spectrum has impor-  
790 tant consequences for the interaction of ULF waves with radiation belt electrons [e.g. *Elkington*  
791 *et al.*, 1999; *Hudson et al.*, 2000; *Elkington et al.*, 2003] and this interaction will be the subject  
792 of future work.

793 **Acknowledgments.** One author (SGC) wishes to thank his thesis advisors, Scot R. Elkington  
794 and Mike Wiltberger, for their outstanding guidance and tutelage. This material is based upon  
795 work supported by the National Aeronautics and Space Administration New Hampshire Space  
796 Grant NNG05GG76H, NASA Grant Nos. NNX08AM34G, NNX08AI36G and by the Center  
797 for Integrated Space Weather Modeling, which is funded by the Science and Technology Centers  
798 program of the National Science Foundation under agreement ATM-0120950.

## References

799 Allan, W., and F. B. Knox (1979a), A dipole field model for axisymmetric Alfvén waves

800 with finite ionosphere conductivities, *Planet. Space Sci.*, 27, 79–85, doi:10.1016/0032-  
801 0633(79)90149-1.

802 Allan, W., and F. B. Knox (1979b), The effect of finite ionosphere conductivities on axisym-  
803 metric toroidal Alfvén wave resonances, *Planet. Space Sci.*, 27, 939–950, doi:10.1016/0032-  
804 0633(79)90024-2.

805 Allan, W., E. M. Poulter, K.-H. Glassmeier, and H. Junginger (1985), Spatial and temporal  
806 structure of a high-latitude transient ULF pulsation, *Planet. Space Sci.*, 33, 159–173, doi:  
807 10.1016/0032-0633(85)90126-6.

808 Allan, W., S. P. White, and E. M. Poulter (1986), Impulse-excited hydromagnetic cavity  
809 and field-line resonances in the magnetosphere, *Planet. Space Sci.*, 34, 371–385, doi:  
810 10.1016/0032-0633(86)90144-3.

811 Anderson, B. J., M. J. Engebretson, S. P. Rounds, L. J. Zanetti, and T. A. Potemra  
812 (1990), A statistical study of Pc 3-5 pulsations observed by the AMPTE/CCE magnetic  
813 fields experiment. I - Occurrence distributions, *J. Geophys. Res.*, 95, 10,495–10,523, doi:  
814 10.1029/JA095iA07p10495.

815 Boris, J. (1970), A physically motivated solution of the Alfvén problem., *NRL Memorandum*  
816 *Report, 2167*, Naval Research Laboratory, Washington DC.

817 Chen, L., and S. C. Cowley (1989), On field line resonances of hydromagnetic Alfvén waves in  
818 dipole magnetic field, *Geophys. Res. Lett.*, 16, 895–897, doi:10.1029/GL016i008p00895.

819 Chen, L., and A. Hasegawa (1974), A theory of long-period magnetic pulsations 1. Steady state  
820 excitation of field line resonance, *J. Geophys. Res.*, 79(7), 1024.

821 Claudepierre, S. G., S. R. Elkington, and M. Wiltberger (2008), Solar wind driving of magne-  
822 tospheric ULF waves: Pulsations driven by velocity shear at the magnetopause, *J. Geophys.*



823 *Res.*, 113(A12), 5218–+, doi:10.1029/2007JA012890.

824 Claudepierre, S. G., M. Wiltberger, S. R. Elkington, W. Lotko, and M. K. Hudson (2009),  
825 Magnetospheric cavity modes driven by solar wind dynamic pressure fluctuations, *Geophys.*  
826 *Res. Lett.*, 36, L13101, doi:10.1029/2009GL039045.

827 Couzens, D., G. K. Parks, K. A. Anderson, R. P. Lin, and H. Reme (1985), ISEE particle  
828 observations of surface waves at the magnetopause boundary layer, *J. Geophys. Res.*, 90,  
829 6343–6353.

830 Dungey, J. W. (1955), Electrodynamics of the Outer Atmosphere, in *Physics of the Ionosphere*,  
831 pp. 229–236.

832 Elkington, S. R., M. K. Hudson, and A. A. Chan (1999), Acceleration of relativistic electrons  
833 via drift-resonant interaction with toroidal-mode Pc-5 ULF oscillations, *Geophys. Res. Lett.*,  
834 26(21), 3273.

835 Elkington, S. R., M. K. Hudson, and A. A. Chan (2003), Resonant acceleration and diffusion of  
836 outer zone electrons in an asymmetric geomagnetic field, *J. Geophys. Res.*, 108(A3), 1116,  
837 doi:10.1029/2001JA009202.

838 Fairfield, D. H. (1979), Global aspects of the Earth's magnetopause, in *Magnetospheric Bound-*  
839 *ary Layers*, *ESA Special Publication*, vol. 148, edited by J. Lemaire, pp. 5–13.

840 Fedder, J. A., S. P. Slinker, J. G. Lyon, and R. D. Elphinstone (1995), Global numerical sim-  
841 ulation of the growth phase and the expansion onset for a substorm observed by Viking, *J.*  
842 *Geophys. Res.*, 100(A10), 19,083–19,093.

843 Fukunishi, H., L. J. Lanzerotti, and C. G. Macleannan (1975), Three-dimensional polarization  
844 characteristics of magnetic variations in the Pc 5 frequency range at conjugate areas near L=4,  
845 *J. Geophys. Res.*, 80, 3973–3984, doi:10.1029/JA080i028p03973.

- 846 Goedbloed, J. P. (1975), Spectrum of ideal magnetohydrodynamics of axisymmetric toroidal  
847 systems, *Phys. Fluids*, *18*, 1258–1268, doi:10.1063/1.861012.
- 848 Gombosi, T. I., D. L. de Zeeuw, K. G. Powell, A. J. Ridley, I. V. Sokolov, Q. F. Stout, and  
849 G. Toth (2003), Adaptive mesh refinement for global magnetohydrodynamic simulation, in  
850 *Space Plasma Simulation, Lecture Notes in Physics, Berlin Springer Verlag*, vol. 615, edited  
851 by J. Büchner, C. Dum, and M. Scholer, pp. 247–274.
- 852 Han, D. S., et al. (2007), Coupling of perturbations in the solar wind density to global Pi3  
853 pulsations: A case study, *J. Geophys. Res.*, *112*(A05217).
- 854 Harrold, B. G., and J. C. Samson (1992), Standing ULF modes of the magnetosphere - A theory,  
855 *Geophys. Res. Lett.*, *19*, 1811–1814.
- 856 Hasegawa, A. (1969), Drift mirror instability of the magnetosphere., *Phys. Fluids*, *12*, 2642–  
857 2650, doi:10.1063/1.1692407.
- 858 Hones, E. W., Jr., S. J. Bame, J. R. Asbridge, J. Birn, G. Paschmann, N. Sckopke, and G. Haeren-  
859 del (1981), Further determination of the characteristics of magnetospheric plasma vortices  
860 with ISEE 1 and 2, *J. Geophys. Res.*, *86*, 814–820.
- 861 Hudson, M. K., S. R. Elkington, J. G. Lyon, and C. C. Goodrich (2000), Increase in relativistic  
862 electron flux in the inner magnetosphere: ULF wave mode structure, *Adv. Space Res.*, *25*(12),  
863 2327.
- 864 Hughes, W. J. (1994), Magnetospheric ULF waves: A tutorial with a historical prespective,  
865 in *Solar wind sources of magnetospheric Ultra-Low-Frequency waves, Geophysical Mono-*  
866 *graphs*, vol. 81, edited by M. Engebretson, K. Takahashi, and M. Scholer, pp. 1–11, AGU,  
867 Washington, DC.

- 868 Hughes, W. J., D. J. Southwood, B. Mauk, R. L. McPherron, and J. N. Barfield (1978),  
869 Alfvén waves generated by an inverted plasma energy distribution., *Nature*, *275*, 43–45, doi:  
870 10.1038/275043a0.
- 871 Inhester, B. (1986), Resonance absorption of Alfvén oscillations in a nonaxisymmetric magne-  
872 tosphere, *J. Geophys. Res.*, *91*, 1509–1518, doi:10.1029/JA091iA02p01509.
- 873 Jacobs, J. A., Y. Kato, S. Matsushita, and V. A. Troitskaya (1964), Classification of geomagnetic  
874 micropulsations, *J. Geophys. Res.*, *69*, 180.
- 875 Kepko, L., and H. E. Spence (2003), Observations of discrete, global magnetospheric oscil-  
876 lations directly driven by solar wind density variations, *J. Geophys. Res.*, *108*(A6), 1257,  
877 doi:10.1029/2002JA009676.
- 878 Kepko, L., H. E. Spence, and H. J. Singer (2002), ULF waves in the solar wind as direct drivers  
879 of magnetospheric pulsations, *Geophys. Res. Lett.*, *29*(8), 39–1, doi:10.1029/2001GL014405.
- 880 Korotova, G. I., and D. G. Sibeck (1995), A case study of transient event motion in the magne-  
881 tosphere and in the ionosphere, *J. Geophys. Res.*, *100*(A1), 35–46.
- 882 Kouznetsov, I., and W. Lotko (1995), Radial energy transport by magnetospheric ULF waves:  
883 Effects of magnetic curvature and plasma pressure, *J. Geophys. Res.*, *100*, 7599–7612, doi:  
884 10.1029/94JA02293.
- 885 Lee, D., and R. L. Lysak (1999), MHD waves in a three-dimensional dipolar magnetic field: A  
886 search for Pi2 pulsations, *J. Geophys. Res.*, *104*, 28,691–28,700, doi:10.1029/1999JA900377.
- 887 Lee, D., K. Kim, R. E. Denton, and K. Takahashi (2004), Effects of ionospheric damping on  
888 MHD wave mode structure, *Earth Planets Space*, *56*.
- 889 Lee, D.-H., and R. L. Lysak (1989), Magnetospheric ULF wave coupling in the dipole model -  
890 The impulsive excitation, *J. Geophys. Res.*, *94*, 17,097–17,103.

- 891 Lee, D.-H., and R. L. Lysak (1991), Impulsive excitation of ULF waves in the three-dimensional  
892 dipole model - The initial results, *J. Geophys. Res.*, *96*, 3479–3486, doi:10.1029/90JA02349.
- 893 Lyon, J. G., J. A. Fedder, and C. M. Mobarry (2004), The Lyon–Fedder–Mobarry (LFM)  
894 global MHD magnetospheric simulation code, *J. Atmos. Solar-Terr. Phys.*, *66*(15), 1333, doi:  
895 10.1016/j.jastp.2004.03.020.
- 896 Matsuoka, H., K. Takahashi, K. Yumoto, B. J. Anderson, and D. G. Sibeck (1995), Observation  
897 and modeling of compressional Pi 3 magnetic pulsations, *J. Geophys. Res.*, *100*(A7), 12,103–  
898 12,115.
- 899 McDiarmid, D. R., A. N. Wright, and W. Allan (1999), Time-limited excitation of damped  
900 field-line resonances: Implications for satellite observations, *J. Geophys. Res.*, *104*, 17,409–  
901 17,418, doi:10.1029/1999JA900184.
- 902 Mond, M., E. Hameiri, and P. N. Hu (1990), Coupling of magnetohydrodynamic waves  
903 in inhomogeneous magnetic field configurations, *J. Geophys. Res.*, *95*, 89–95, doi:  
904 10.1029/JA095iA01p00089.
- 905 Newton, R. S., D. J. Southwood, and W. J. Hughes (1978), Damping of geomagnetic pulsations  
906 by the ionosphere, *Planet. Space Sci.*, *26*, 201–209, doi:10.1016/0032-0633(78)90085-5.
- 907 Ozeke, L. G., and I. R. Mann (2004), Modeling the properties of guided poloidal Alfvén  
908 waves with finite asymmetric ionospheric conductivities in a dipole field, *J. Geophys. Res.*,  
909 *109*(A18), 5205–+, doi:10.1029/2003JA010151.
- 910 Percival, D. B., and A. T. Walden (1993), *Spectral Analysis for Physical Applications*, 580 pp.,  
911 Cambridge University.
- 912 Potemra, T. A., L. J. Zanetti, K. Takahashi, H. Luehr, and R. P. Lepping (1989), Multisatellite  
913 and ground-based observations of transient ULF waves, *J. Geophys. Res.*, *94*, 2543–2554,

914 doi:10.1029/JA094iA03p02543.

915 Press, W. H., S. A. Teukolsky, W. T. Vetterling, and B. P. Flannery (1992), *Numerical recipes*  
916 *in Fortran 77: The art of scientific computing, Fortran Numerical Recipes*, vol. 1, 2 ed., 922  
917 pp., Cambridge Univ. Press, New York.

918 Pu, Z.-Y., and M. G. Kivelson (1983), Kelvin-Helmholtz instability at the magnetopause: Solu-  
919 tion for compressible plasmas, *J. Geophys. Res.*, 88(A2), 841–852.

920 Radoski, H. R. (1966), Magnetic Toroidal Resonances and Vibrating Field Lines, *J. Geophys.*  
921 *Res.*, 71, 1891–+.

922 Radoski, H. R. (1974), A Theory of Latitude Dependent Geomagnetic Micropulsations: The  
923 Asymptotic Fields, *J. Geophys. Res.*, 79, 595–603, doi:10.1029/JA079i004p00595.

924 Radoski, H. R., and R. L. Carovillano (1966), Axisymmetric Plasmasphere Resonances:  
925 Toroidal Mode, *Phys. Fluids*, 9, 285–291, doi:10.1063/1.1761671.

926 Raeder, J., Y. Wang, and T. J. Fuller-Rowell (2001), Geomagnetic storm simulation with a cou-  
927 pled magnetosphere- ionosphere-thermosphere model, in *Space Weather, Geophysical Mono-*  
928 *graph Series*, vol. 125, edited by H. Singer, pp. 377–384, AGU.

929 Richmond, A. D. (1992), Assimilative mapping of ionospheric electrodynamics, *Adv. Space*  
930 *Res.*, 12, 59–68, doi:10.1016/0273-1177(92)90040-5.

931 Rickard, G. J., and A. N. Wright (1994), Alfvén resonance excitation and fast wave propagation  
932 in magnetospheric waveguides, *J. Geophys. Res.*, 99, 13,455–+, doi:10.1029/94JA00674.

933 Rickard, G. J., and A. N. Wright (1995), ULF pulsations in a magnetospheric waveguide:  
934 Comparison of real and simulated satellite data, *J. Geophys. Res.*, 100, 3531–3537, doi:  
935 10.1029/94JA02935.

- 936 Rostoker, G., and B. T. Sullivan (1987), Polarization characteristics of Pc5 magnetic pulsations  
937 in the dusk hemisphere, *Planet. Space Sci.*, *35*, 429–438, doi:10.1016/0032-0633(87)90099-  
938 7.
- 939 Ruohoniemi, J. M., R. A. Greenwald, K. B. Baker, and J. C. Samson (1991), HF radar obser-  
940 vations of Pc 5 field line resonances in the midnight/early morning MLT sector, *J. Geophys.*  
941 *Res.*, *96*, 15,697–+.
- 942 Samson, J. C., and G. Rostoker (1972), Latitude-Dependent Characteristics of High-  
943 Latitude Pc 4 and Pc 5 Micropulsations, *J. Geophys. Res.*, *77*, 6133–6144, doi:  
944 10.1029/JA077i031p06133.
- 945 Samson, J. C., J. A. Jacobs, and G. Rostoker (1971), Latitude-Dependent Characteristics  
946 of Long-Period Geomagnetic Micropulsations, *J. Geophys. Res.*, *76*, 3675–3683, doi:  
947 10.1029/JA076i016p03675.
- 948 Samson, J. C., B. G. Harrold, J. M. Ruohoniemi, R. A. Greenwald, and A. D. M. Walker (1992),  
949 Field line resonances associated with MHD waveguides in the magnetosphere, *Geophys. Res.*  
950 *Lett.*, *19*, 441–444.
- 951 Sarafopoulos, D. V. (1995), Long duration Pc 5 compressional pulsations inside the Earth's  
952 magnetotail lobes, *Ann. Geophys.*, *13*, 926–937.
- 953 Sckopke, N., G. Paschmann, G. Haerendel, B. U. O. Sonnerup, S. J. Bame, T. G. Forbes, E. W.  
954 Hones, and C. T. Russell (1981), Structure of the low-latitude boundary layer, *J. Geophys.*  
955 *Res.*, *86*, 2099.
- 956 Singer, H. J., C. T. Russell, M. G. Kivelson, T. A. Fritz, and W. Lennartsson (1979), Satellite ob-  
957 servations of the spatial extent and structure of Pc 3, 4, 5 pulsations near the magnetospheric  
958 equator, *Geophys. Res. Lett.*, *6*, 889–892, doi:10.1029/GL006i011p00889.

- 959 Singer, H. J., D. J. Southwood, R. J. Walker, and M. G. Kivelson (1981), Alfvén wave reso-  
960 nances in a realistic magnetospheric magnetic field geometry, *J. Geophys. Res.*, *86*, 4589–  
961 4596, doi:10.1029/JA086iA06p04589.
- 962 Southwood, D. J. (1974), Some features of field line resonances in the magnetosphere, *Planet.*  
963 *Space Sci.*, *22*, 483–491.
- 964 Southwood, D. J., and W. J. Hughes (1983), Theory of hydromagnetic waves in the magneto-  
965 sphere, *Space Sci. Rev.*, *35*(4), 301–366.
- 966 Southwood, D. J., and M. G. Kivelson (1986), The effect of parallel inhomogeneity on  
967 magnetospheric hydromagnetic wave coupling, *J. Geophys. Res.*, *91*, 6871–6876, doi:  
968 10.1029/JA091iA06p06871.
- 969 Southwood, D. J., and M. G. Kivelson (1990), The magnetohydrodynamic response of the mag-  
970 netospheric cavity to changes in solar wind pressure, *J. Geophys. Res.*, *95*, 2301–2309, doi:  
971 10.1029/JA095iA03p02301.
- 972 Stellmacher, M., K. Glassmeier, R. L. Lysak, and M. G. Kivelson (1997), Field line resonances  
973 in discretized magnetospheric models: an artifact study., *Ann. Geophys.*, *15*, 614–624.
- 974 Stephenson, J. A. E., and A. D. M. Walker (2002), HF radar observations of Pc5 ULF pulsations  
975 driven by the solar wind, *Geophys. Res. Lett.*, *29*(9), 1297.
- 976 Takahashi, K., and R. L. McPherron (1984), Standing hydromagnetic oscillations in the magne-  
977 tosphere, *Planet. Space Sci.*, *32*, 1343–1359.
- 978 Takahashi, K., and A. Y. Ukhorskiy (2007), Solar wind control of Pc5 pulsation power at  
979 geosynchronous orbit, *J. Geophys. Res.*, *112*(A11205).
- 980 Takahashi, K., T. A. Potemra, R. W. McEntire, L. J. Zanetti, and L. M. Kistler (1988), Magne-  
981 topheric ULF waves observed during the major magnetospheric compression of November

- 982 1, 1984, *J. Geophys. Res.*, *93*, 14,369–14,382, doi:10.1029/JA093iA12p14369.
- 983 Thomson, D. J. (1982), Spectrum estimation and harmonic analysis, *Proc. IEEE*, *70*, 1055–  
984 1096.
- 985 Viall, N. M., L. Kepko, and H. E. Spence (2009), Relative occurrence rates and connection  
986 of discrete frequency oscillations in the solar wind density and dayside magnetosphere, *J.*  
987 *Geophys. Res.*, *114*(A13), 1201–+, doi:10.1029/2008JA013334.
- 988 Walker, A. D. M. (1981), The Kelvin-Helmholtz instability in the low-latitude boundary layer,  
989 *Planet. Space Sci.*, *29*(10), 1119–1133.
- 990 Walker, A. D. M., R. A. Greenwald, W. F. Stuart, and C. A. Green (1979), STARE auroral  
991 radar observations of Pc 5 geomagnetic pulsations, *J. Geophys. Res.*, *84*, 3373–3388, doi:  
992 10.1029/JA084iA07p03373.
- 993 Warner, M. R., and D. Orr (1979), Time of flight calculations for high latitude geomagnetic  
994 pulsations, *Planet. Space Sci.*, *27*, 679–689, doi:10.1016/0032-0633(79)90165-X.
- 995 Wiltberger, M., R. E. Lopez, and J. G. Lyon (2005), Results from magnetospheric Gedanken  
996 experiments using the LFM, *Adv. Space Res.*, *36*, 1797–1803, doi:10.1016/j.asr.2004.11.043.
- 997 Wiltberger, M., R. S. Weigel, W. Lotko, and J. A. Fedder (2009), Modeling seasonal variations  
998 of auroral particle precipitation in a global-scale magnetosphere-ionosphere simulation, *J.*  
999 *Geophys. Res.*, *114*(A13), 1204–+, doi:10.1029/2008JA013108.
- 1000 Wright, A. N. (1992), Coupling of fast and Alfvén modes in realistic magnetospheric geome-  
1001 tries, *J. Geophys. Res.*, *97*, 6429–6438, doi:10.1029/91JA02655.
- 1002 Wright, A. N. (1994), Dispersion and wave coupling in inhomogeneous MHD waveguides, *J.*  
1003 *Geophys. Res.*, *99*, 159–167, doi:10.1029/93JA02206.



- 1004 Wright, A. N., and G. J. Rickard (1995), A numerical study of resonant absorption in a mag-  
1005 netohydrodynamic cavity driven by a broadband spectrum, *Astrophys. J.*, *444*, 458–470, doi:  
1006 10.1086/175620.
- 1007 Wright, A. N., and M. J. Thompson (1994), Analytical treatment of Alfvén resonances  
1008 and singularities in nonuniform magnetoplasmas, *Phys. Plasmas*, *1*, 691–705, doi:  
1009 10.1063/1.870815.
- 1010 Yumoto, K., and T. Saito (1983), Relation of compressional HM waves at GOES 2  
1011 to low-latitude Pc 3 magnetic pulsations, *J. Geophys. Res.*, *88*, 10,041–10,052, doi:  
1012 10.1029/JA088iA12p10041.
- 1013 Zhu, X., and M. G. Kivelson (1989), Global mode ULF pulsations in a magnetosphere  
1014 with a nonmonotonic Alfvén velocity profile, *J. Geophys. Res.*, *94*, 1479–1485, doi:  
1015 10.1029/JA094iA02p01479.

Run	Field line A		Field line B	
	Cartesian	Polar	Cartesian	Polar
10 mHz	(5.0, 5.0, 0)	(7.1, 45°, 0)	-	-
15 mHz	(4.6, 4.6, 0)	(6.5, 45°, 0)	(6.5, 6.5, 0)	(9.2, 45°, 0)
25 mHz	(4.1, 4.1, 0)	(5.8, 45°, 0)	(5.9, 5.9, 0)	(8.3, 45°, 0)

**Table 1.** Locations of the field lines used in the FLR mode structure calculations for the three monochromatic simulations. The point where the field line intersects the equatorial plane is given in Cartesian,  $(x, y, z)$ , and cylindrical polar,  $(r, \varphi, z)$ , coordinates. All units are in  $R_E$  except  $\varphi$ , which is in degrees.

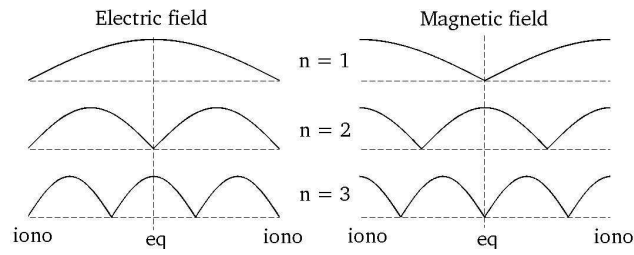


**Figure 1.** Oscillation amplitude schematics for resonant standing waves on straight magnetic field lines bounded by perfect conductors representing geomagnetic field lines bounded by the ionosphere. Electric and magnetic field oscillation amplitudes are shown for the fundamental mode and the second and third harmonics. To facilitate the comparisons with our simulation results, oscillation amplitude is plotted as a non-negative quantity. The field line foot points are assumed to lie in a perfectly conducting ionosphere (labeled ‘iono’). The location of the geomagnetic equatorial plane is indicated by a vertical dashed line in each column (labeled ‘eq’).

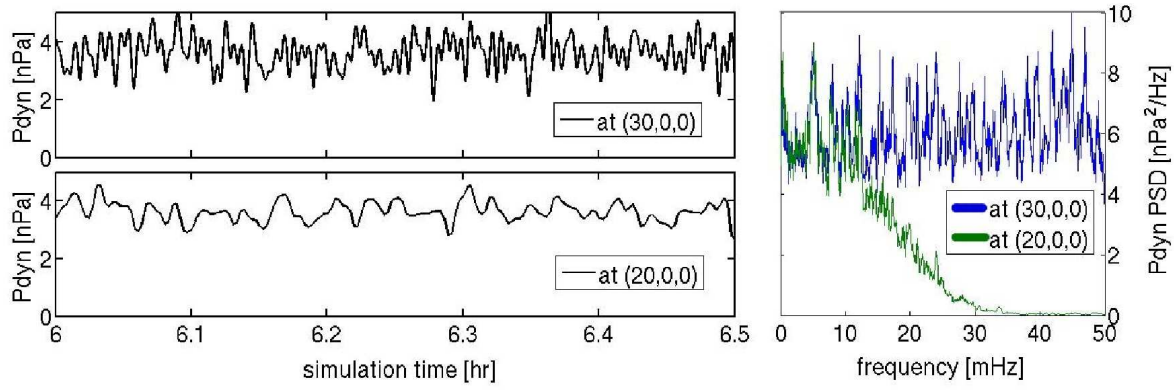


**Figure 2.** Solar wind dynamic pressure driving in the continuum simulation. The two time series on the left show the dynamic pressure input into the simulation at the upstream boundary (at  $\mathbf{x} = (30,0,0) R_E$ , top panel) and the resultant dynamic pressure in the upstream solar wind in the simulation  $10 R_E$  downstream (at  $\mathbf{x} = (20,0,0) R_E$ , bottom panel). Note that the higher frequency fluctuations in the input time series are filtered out by the time the fluctuations reach  $\mathbf{x} = (20,0,0) R_E$  in the simulation. The blue and green traces in the right panel are the power spectral densities of the two time series shown on the left, illustrating the high frequency filtering. The green trace is the spectral profile that drives the magnetosphere in the continuum simulation.

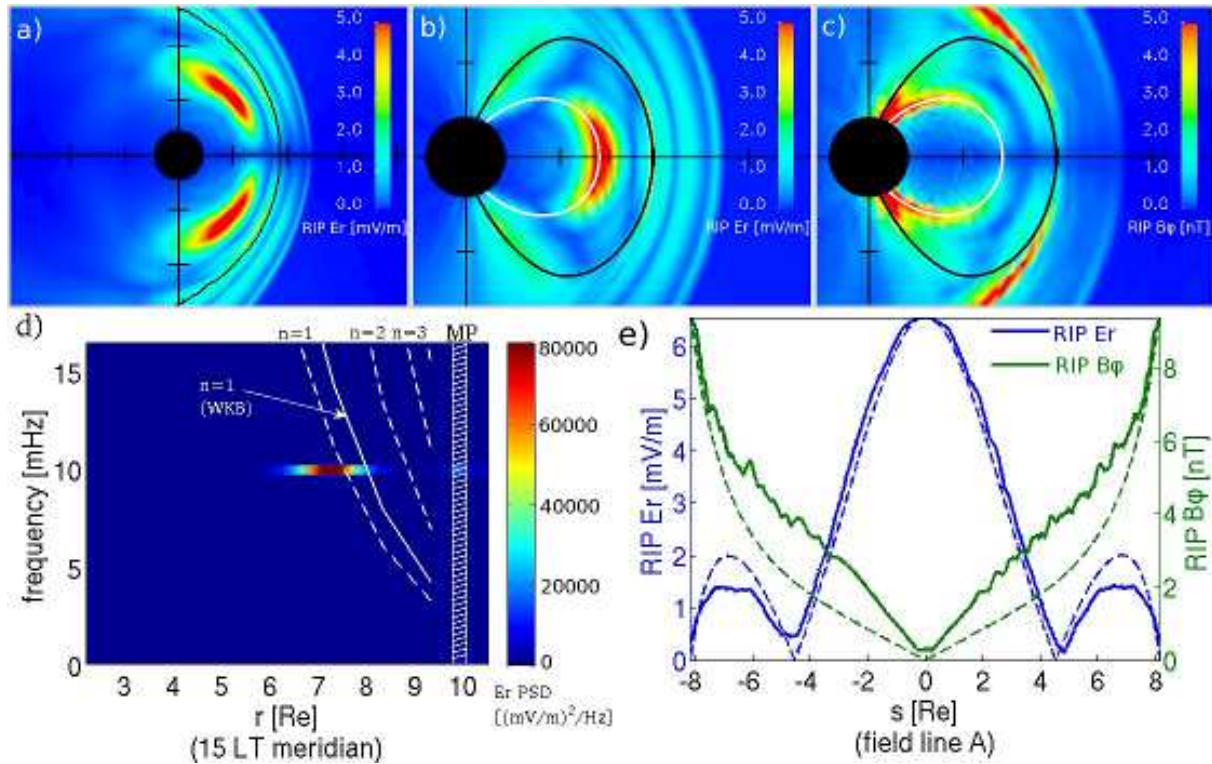


**Figure 3.** Summary of results from the 10 mHz monochromatic simulation. **a)** Equatorial plane distribution of driving band ([9.5,10.5] mHz)  $E_r$  root-integrated power (RIP). **b)** Distribution of driving band  $E_r$  RIP in the 15 LT meridional plane. The white field line is field line A in the 10 mHz simulation and the black field line is the last closed field line in the 15 LT meridional plane. Field line A intersects the equatorial plane at  $r = 7.1 R_E$  on the 15 LT meridian. **c)** Distribution of driving band  $B_\phi$  RIP in the 15 LT meridional plane. The same two field lines from panel b) are shown. **d)** Radial profile of  $E_r$  power spectral density along the 15 LT meridian. The dashed white traces are the field line eigenfrequency profiles (dipole estimate) and the location of the magnetopause is indicated by the white shaded region near  $10 R_E$ . The  $n = 1$  WKB eigenfrequency estimate is also shown for comparison (solid white trace). **e)**  $E_r$  (solid blue) and  $B_\phi$  (solid green) mode structure profiles along field line A. The two solid traces can be compared with panels b) and c), where field line A is shown in white. The dashed traces are the theoretical mode structure profiles for fundamental toroidal mode FLR oscillations in  $E_r$  and  $B_\phi$  and are discussed in greater detail in Section 4.1. Note the fundamental toroidal mode field line resonance excited near September 12, 2018, the entire dayside, excluding near the noon meridian.

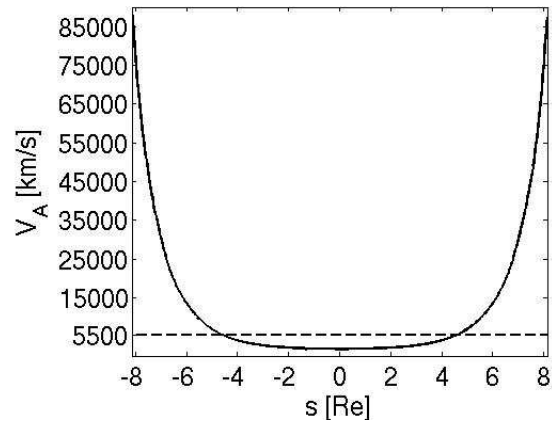


**Figure 4.** Alfvén speed profile along field line A in the 10 mHz monochromatic simulation (solid trace). The dashed trace marks 5,500 km/s, the value of the Boris corrected speed of light in the LFM simulation. Note that in the vicinity of the equatorial plane, the local Alfvén speed is less than the speed of light in the LFM simulation.

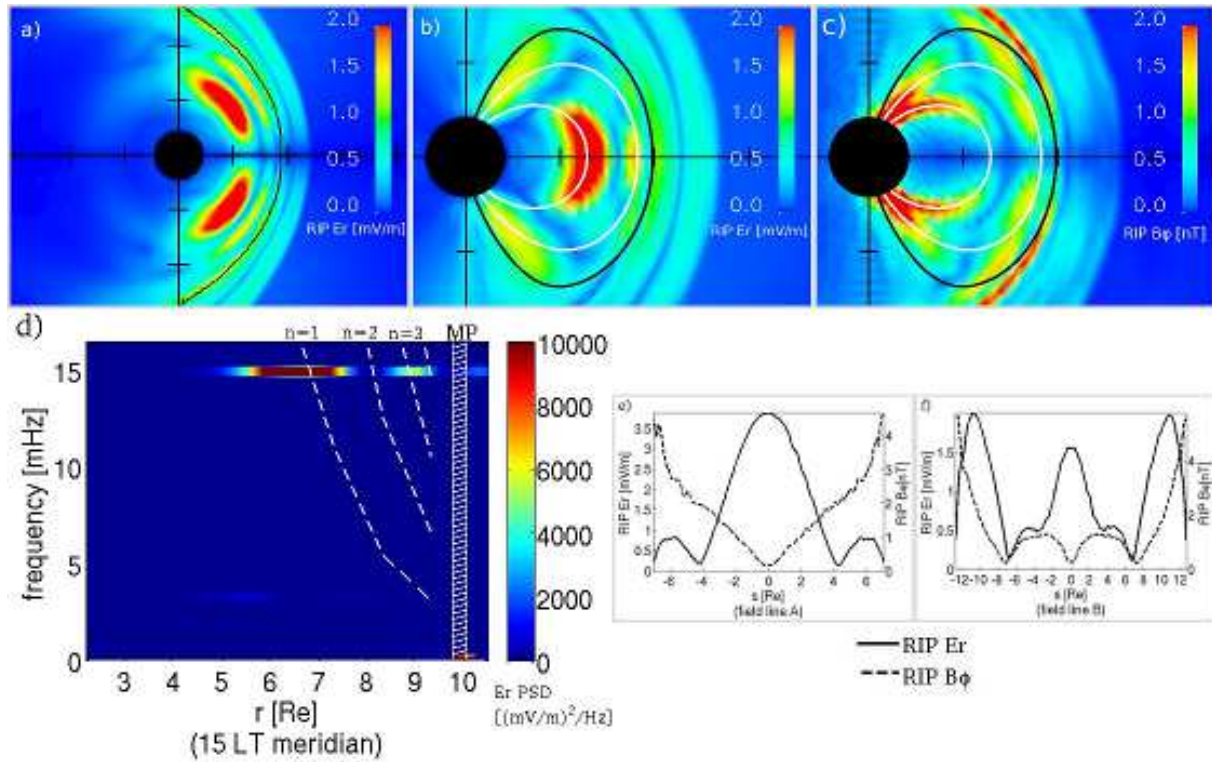


**Figure 5.** Summary of results from the 15 mHz monochromatic simulation. **a)** Equatorial plane distribution of driving band ([14.5,15.5] mHz)  $E_r$  root-integrated power (RIP). **b)** Distribution of driving band  $E_r$  RIP in the 15 LT meridional plane. The two white field lines are field lines A and B in the 15 mHz simulation and the black field line is the last closed field line in the 15 LT meridional plane. Field line A intersects the equatorial plane at  $r = 6.5 R_E$  on the 15 LT meridian and field line B intersects at  $r = 9.2 R_E$ . **c)** Distribution of driving band  $B_\phi$  RIP in the 15 LT meridional plane. The same three field lines from panel b) are shown. **d)** Radial profile of  $E_r$  power spectral density along the 15 LT meridian. The dashed white traces are the field line eigenfrequency profiles (dipole estimate) and the location of the magnetopause is indicated by the white shaded region near  $10 R_E$ . **e)**  $E_r$  and  $B_\phi$  mode structure profiles along field line A. The two traces can be compared with panels b) and c), where field line A is shown in white. **f)**  $E_r$  and  $B_\phi$  mode structure profiles along field line B. The two traces can be compared with panels b) and c), where field line B is shown in white. Note the  $n = 1$  and  $n = 3$  toroidal mode field line resonances excited across most of the dayside, near  $r = 6.5$  and  $9.2 R_E$ , respectively.

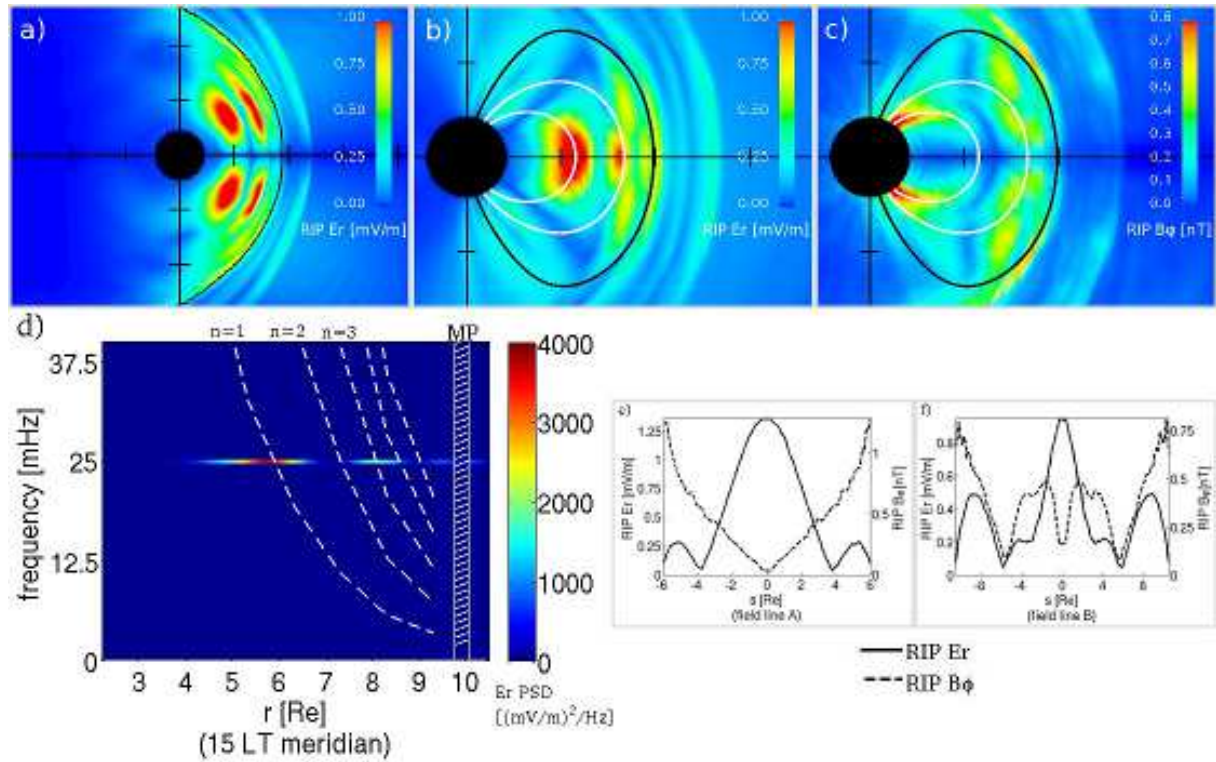


**Figure 6.** Summary of results from the 25 mHz monochromatic simulation. **a)** Equatorial plane distribution of driving band ( $[24.5, 25.5]$  mHz)  $E_r$  root-integrated power (RIP). **b)** Distribution of driving band  $E_r$  RIP in the 15 LT meridional plane. The two white field lines are field lines A and B in the 25 mHz simulation and the black field line is the last closed field line in the 15 LT meridional plane. Field line A intersects the equatorial plane at  $r = 5.8 R_E$  on the 15 LT meridian and field line B intersects at  $r = 8.3 R_E$ . **c)** Distribution of driving band  $B_\phi$  RIP in the 15 LT meridional plane. The same three field lines from panel b) are shown. **d)** Radial profile of  $E_r$  power spectral density along the 15 LT meridian. The dashed white traces are the field line eigenfrequency profiles (dipole estimate) and the location of the magnetopause is indicated by the white shaded region near  $10 R_E$ . **e)**  $E_r$  and  $B_\phi$  mode structure profiles along field line A. The two traces can be compared with panels b) and c), where field line A is shown in white. **f)**  $E_r$  and  $B_\phi$  mode structure profiles along field line B. The two traces can be compared with panels b) and c), where field line B is shown in white. Note the  $n = 1$  and  $n = 3$  toroidal mode field line resonances excited across most of the dayside, near  $r = 5.8$  and  $8.3 R_E$ , respectively.



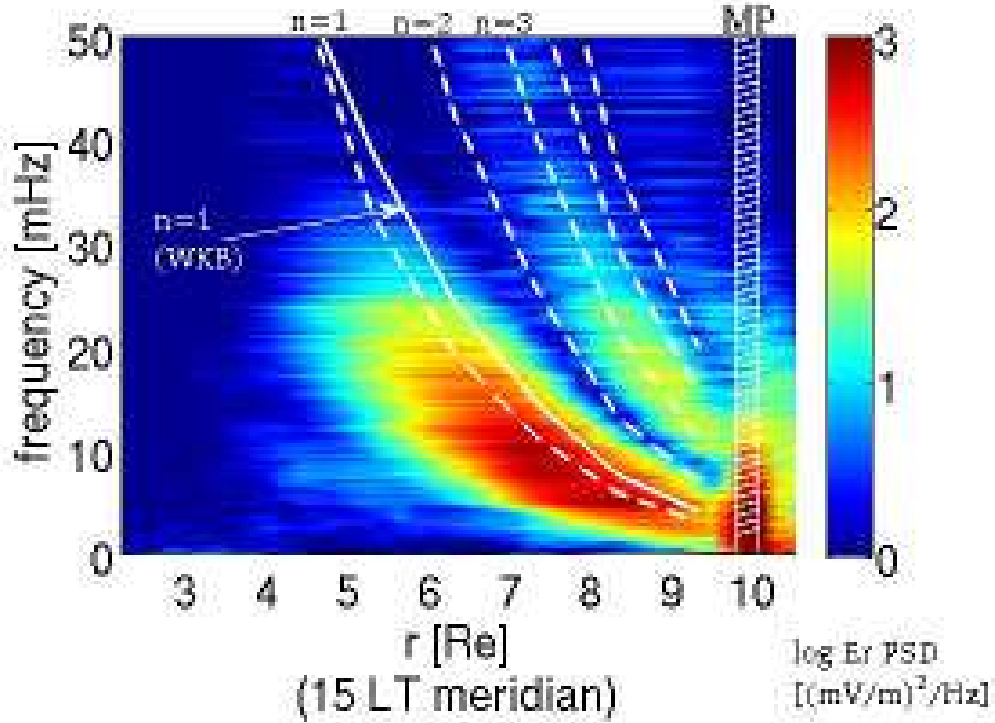


**Figure 7.** Summary of results from the continuum simulation showing the radial profile of  $E_r$  power spectral density along the 15 LT meridian, on a logarithmic color scale. The dashed white traces are the field line eigenfrequency profiles (dipole estimate) and the location of the magnetopause is indicated by the white shaded region near  $10 R_E$ . The  $n = 1$  WKB eigenfrequency estimate is also shown for comparison (solid white trace). Note the continuous spectrum of the  $n = 1$  and  $n = 3$  toroidal mode field line resonances excited along the 15 LT meridian.

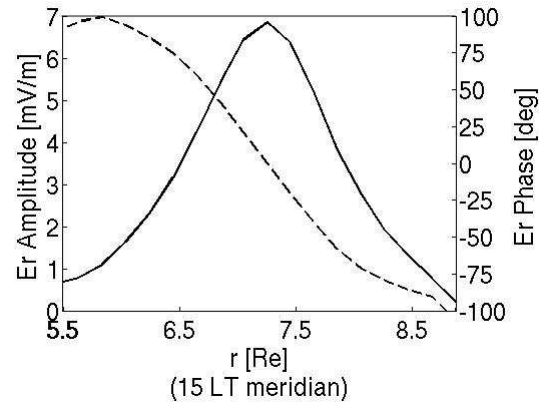


**Figure 8.** Radial electric field amplitude (solid) and phase (dashed) for the fundamental mode FLR in the 10 mHz simulation. Radial distance,  $r$ , along the 15 LT meridian is plotted on the horizontal scale from 5.5 to 8.9  $R_E$ .  $E_r$  driving band  $RIP$  (labeled ‘ $E_r$  amplitude’) is plotted on the left vertical scale from 0 to 7 mV/m and relative phase is plotted on the right vertical scale from  $-100$  to 100 degrees. Note the approximately  $180^\circ$  change in phase across the peak in wave power.

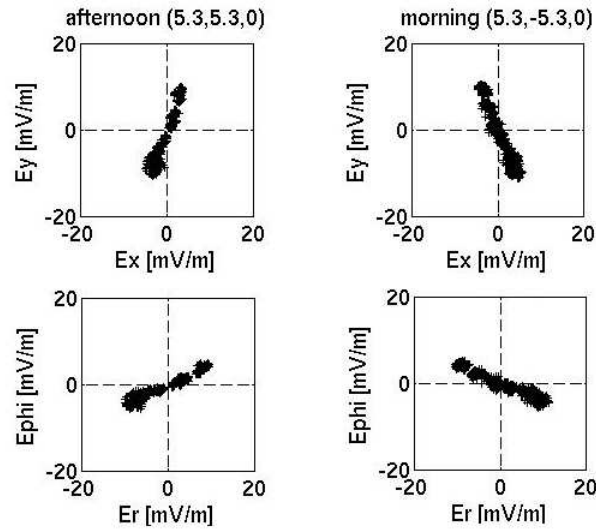


**Figure 9.** Electric field hodograms near the location of the fundamental mode FLR in the 10 mHz simulation. The left column shows the hodograms in the afternoon sector and the right column shows the hodograms in the morning sector. The top row shows the Cartesian coordinate electric field components,  $E_x$  and  $E_y$ , and the bottom row shows the polar coordinate components,  $E_r$  and  $E_\varphi$ . Note the linearly polarized oscillations at the locations of the resonance and the polarization reversal across the noon meridian.

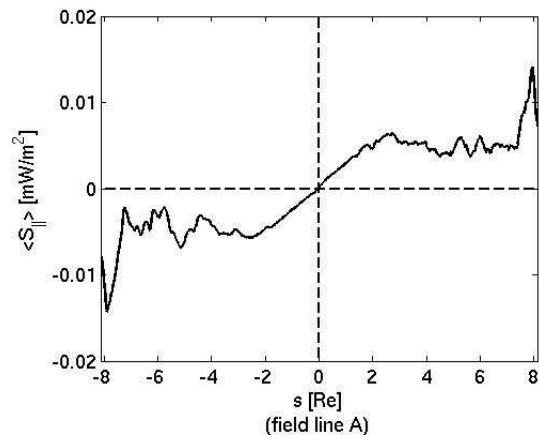


**Figure 10.** Parallel component of the time averaged Poynting vector along field line A in the 10 mHz simulation. Note the net flux of energy out of the equatorial plane, towards the northern and southern ionospheres.